

SPITZER OBSERVATIONS OF PASSIVE AND STAR FORMING EARLY-TYPE GALAXIES: AN INFRARED COLOR-COLOR SEQUENCE

Pasquale Temi^{1,2}, Fabrizio Brighenti^{3,4}, William G. Mathews³

ABSTRACT

We describe the infrared properties of a large sample of early type galaxies, comparing data from the Spitzer archive with Ks -band emission from 2MASS. While most representations of this data result in correlations with large scatter, we find a remarkably tight relation among colors formed by ratios of luminosities in Spitzer-MIPS bands (24, 70 and $160\mu\text{m}$) and the Ks -band. Remarkably, this correlation among E and S0 galaxies follows that of nearby normal galaxies of all morphological types. In particular, the tight infrared color-color correlation for S0 galaxies alone follows that of the entire Hubble sequence of normal galaxies, roughly in order of galaxy type from ellipticals to spirals to irregulars. The specific star formation rate of S0 galaxies estimated from the $24\mu\text{m}$ luminosity increases with decreasing K -band luminosity (or stellar mass) from essentially zero, as with most massive ellipticals, to rates typical of irregular galaxies. Moreover, the luminosities of the many infrared-luminous S0 galaxies can significantly exceed those of the most luminous (presumably post-merger) E galaxies. Star formation rates in the most infrared-luminous S0 galaxies approach 1–10 solar masses per year. Consistently with this picture we find that while most early-type galaxies populate an infrared red sequence, about 24% of the objects (mostly S0s) are in an infrared blue cloud together with late type galaxies. For those early-type galaxies also observed at radio frequencies we find that the far-infrared luminosities correlate with the mass of neutral and molecular hydrogen, but the scatter is large. This scatter suggests that the star formation may be intermittent or that similar S0 galaxies with cold gaseous disks of nearly equal mass can have varying radial column density distributions that alter the local and global star formation rates.

Subject headings: galaxies: elliptical and lenticular

1. Introduction

If S0 galaxies did not exist it is possible that they would not have been missed. Late type, star-

forming galaxies including spirals are expected in early galactic evolution and elliptical galaxies are thought to form by mergers among these ancient late type galaxies or, at a later stage, from dry mergers with each other. S0 or lenticular galaxies are differentiated from these more predictable and recognizable galaxies by being generally structureless with stellar bulges and rotating disks having light distributions that are somewhat less concentrated than in ellipticals. The distinction between E and S0 morphologies is not always easy, particularly when S0s are viewed face-on. This classification difficulty has resulted in the notion of E-S0 galaxies where the uncertain type may either be an intrinsic reality or a consequence of the limita-

¹Astrophysics Branch, NASA/Ames Research Center, MS 245-6, Moffett Field, CA 94035 (pasquale.temi@nasa.gov).

² Department of Physics and Astronomy, University of Western Ontario, London, ON N6A 3K7, Canada.

³University of California Observatories/Lick Observatory, Board of Studies in Astronomy and Astrophysics, University of California, Santa Cruz, CA 95064 (mathews@ucolick.org).

⁴Dipartimento di Astronomia, Università di Bologna, via Ranzani 1, Bologna 40127, Italy (fabrizio.brighenti@unibo.it).

tions of the astronomical classifier. S0s are often a nuisance in large surveys since the S0-E distinction decreases with redshift and the two types of galaxies are often combined.

However, many local S0 galaxies are quite distinct from ellipticals, particularly as a result of their significant gas content, star formation rates, and optical colors. At infrared wavelengths many S0 galaxies exhibit a range of unusual properties not often found in ellipticals.

Recently we discussed the infrared properties of 34 S0 and E galaxies in the SAURON sample that have also been observed in the infrared with the Spitzer telescope (Temi, Brighenti & Mathews 2009; hereafter TBM09). This relatively small Spitzer-SAURON sample is useful since SAURON galaxies have been intensively observed at many other wavelengths. While the infrared emission from some S0 galaxies in the Spitzer-SAURON sample closely resembles gas-free elliptical galaxies, many S0 galaxies contain rotationally supported kpc-sized disks of star-forming cold gas (e.g. Combes, Young & Bureau 2007; Young, Bendo & Lucero 2009) and dust that emit more strongly in Spitzer bandpasses than ellipticals. The star formation rates in S0s in the Spitzer-SAURON sample, derived from their $24\mu\text{m}$ emission, are small, $\lesssim 0.2 M_{\odot} \text{ yr}^{-1}$, but correlate with the magnitude of the $H\beta$ spectral index produced by relatively young A-F stars (TBM09). However, in SAURON S0 galaxies we found that star formation rates estimated from Balmer emission line luminosities are often much less than star formation rates found from $24\mu\text{m}$ emission. The insufficient emission line evidence for OB stars is curious since slightly less massive young stars are often visible. In any case, hydrogen line emission is easily absorbed by dust, so estimates of star formation rates in S0 galaxies are probably more reliably determined from $24\mu\text{m}$ dust emission or by a combination of $H\alpha$ and infrared luminosities (Kennicutt et al. 2009)

In this paper we discuss infrared Spitzer observations of a much larger, more comprehensive sample of E and S0 galaxies taken from the Spitzer archive. This extended sample reveals some remarkable attributes of S0 galaxies. Most important of these is a very narrow correlation between colors formed by ratios of mid and far-infrared Spitzer luminosities with K -band luminosities in

which the dust properties differentiate many but not all S0s from gas-free E galaxies. Furthermore, it is remarkable that the color-color correlation for S0s is nearly identical to that of normal galaxies spanning all morphological types. Although ancillary data is less abundant for this extended sample of early-type galaxies than for the SAURON-Spitzer sample, the mass of neutral and molecular hydrogen is known for many of them and this provides several interesting comparisons with star formation rates based on their Spitzer $24\mu\text{m}$ luminosities.

2. Spitzer Observations of Early Type Galaxies

Table 1 contains relevant information about our extended sample of elliptical and lenticular galaxies found from the Spitzer archives. We searched the archives to select early-type galaxies within a distance of 30 Mpc that have been observed with Spitzer at far infrared wavelengths. About 60 more distant galaxies have been added from known Spitzer observing programs and by querying large lists of early-type galaxies known from other surveys. Of the 225 galaxies in Table 1, 121 are ellipticals, 26 are E-S0 and 76 are S0. Two galaxies have uncertain classification (NGC 3656 and NGC 5666). NGC 5666 was classified as an elliptical in early studies by Nilson (1973) and Lake et al. (1987). Recently Donzelli & Davoust (2003) found evidence of spiral structures from deep CCD images, suggesting a late type Sc galaxy. However photometric analysis indicates a number of contradictory morphological properties that point toward a classification of an early type disk galaxy which has accreted a gas rich dwarf galaxy during a minor merger event. NGC 3656 is classified as (R')I0: pec by NED. Its morphological classification is not reported in the HyperLeda catalog, and is listed as non-Magellanic irregular in RC2 catalog. From near infrared photometry, Wiklind, Combes & Henkel (1995) classify NGC3656 as a disturbed elliptical with an envelope of faint shells and a dust lane. They point out that it could be also considered a face-on S0. None of our results changes if these two galaxy are removed from the sample. This table also includes all early-type galaxies in our proprietary Spitzer observations (Temi, Brighenti & Mathews 2007, hereafter TBM07) as well as early-type SAURON galaxies

observed with Spitzer and discussed in TBM09. All but four galaxies in Table 1 are massive or relatively massive, i.e. $\text{Log}L_{Ks} > 8.4$ ($M_{Ks} < -17.6$). Table 1 contains flux densities and specific luminosities L_λ at 24, 70 and $160\mu\text{m}$.¹

3. Observations and Reduction

The FIR data presented here were obtained with the Multiband Imaging Photometer (MIPS; Rieke et al. 2004) on board the Spitzer Space Telescope (SST ; Werner et al. 2004) in three wavebands centered at 24, 70, and $160\mu\text{m}$. These data, collected from the Spitzer public archive, do not form a homogeneous and uniform data set in terms of image depth and observing mode. Column 2 of Table 1 lists the program identification (ID) and principal investigator (PI) for the various original Spitzer observing programs from which our sample galaxies are selected. The reader is referred to these programs to obtain details on the observing modes and imaging strategy, as well as the on-source integration time for each target in the sample. As an example, Virgo Cluster galaxies recorded under the guaranteed time program (PID 69, PI G. Fazio) reach a relatively low sensitivity of 0.5 MJy sr^{-1} and 1.1 MJy sr^{-1} (1σ) at 70 and $160\mu\text{m}$, respectively, while other galaxies (i.e., PID 20171, PI P. Temi) have deeper maps at a sensitivity level of only 0.12 MJy sr^{-1} and 0.3 MJy sr^{-1} for the same two wavebands. The Spitzer Infrared Nearby Galaxies Survey (SINGS) data are recorded in MIPS scan mode, covering a very large sky area ($30' \times 10'$), incorporating two separated passes at each source location. SINGS images correspond to maps with intermediate sensitivity. Apart from the SINGS observations, data have been acquired in MIPS photometry mode, allowing appropriate coverage of the sources and their extended emission.

Reduction of data from the Spitzer archives follows the same procedure used in Temi et al. (2007). Here, we briefly summarize the basic processes involved. We started with the Basic Calibrated Data (BCD) products from the Spitzer Science pipeline (version 16.1) to construct mosaic images for all objects. Final calibrated im-

ages have been produced using the Mosaicking and Point-source Extraction (MOPEX) package developed at the Spitzer Science Center (Makovoz et al. 2006). MOPEX includes all the functions and steps necessary to process BCD data into corrected images and co-add them into a mosaic. The major MOPEX pipeline used was the mosaic pipeline which consists of a number of individual modules to be run in sequence to properly perform the reduction. We refer the reader to the MOPEX web page for a detailed description of each module. Since the data sets presented here have been acquired in different observing modes, the modules chosen to buildup the reduction flow and their parameter setup have been carefully selected to properly remove mode-dependent artifacts in the final mosaic (outlier detection and median filtering). Data reduction presented here make use of the most updated MIPS flux calibration factors based on a large sample of stars and asteroids (Engelbracht et al. 2007; Gordon et al. 2007; Stansberry et al 2007).

Foreground stars and background galaxies present in the original mosaiced images were deleted before flux extraction was performed. These were identified by eye and cross-checked using surveys at other wavelengths (Digital Sky Survey and 2MASS). Flux densities were extracted from apertures that cover the entire optical disk (R25). Sky subtraction was performed by averaging values from multiple apertures placed around the target, avoiding any overlap with the faint extended emission from the galaxy. Statistical uncertainties related to sky subtraction are usually less than 1% but can be appreciable (tens of percent) for faint sources. Observed infrared flux densities for each galaxy are listed in Table 1. Columns 10-12 contain the specific flux F_λ (mJy) identified by each MIPS wavelength 24, 70, and $160\mu\text{m}$.

Systematics in the MIPS calibration result in fluxes uncertain at the 5% level at $24\mu\text{m}$ and 10% at 70 and 15% at $160\mu\text{m}$. The uncertainties listed in Table 1 include the systematic uncertainties. Aperture corrections for extended sources were applied to the fluxes as described in the Spitzer Observer's Manual. The corresponding MIPS luminosities are $L_\lambda = \lambda F_\lambda \cdot 4\pi D^2$, where distances D are from Table 1.

¹In this paper L_λ represents λL_λ in erg s^{-1} . This differs from our previous notation in which L_λ represented the Spitzer band width multiplied by the specific luminosity.

4. Infrared Photometry of E and S0 Galaxies

Figure 1 shows the luminosities in three Spitzer bandpasses plotted against the Ks -band luminosity L_{Ks} . The tight correlation among the elliptical galaxies (filled red circles) in the upper panel is expected from an old stellar population in which most of the warmer dust emitting at $24\mu\text{m}$ is in circumstellar outflows from old red giant stars. The correlation visible in this panel is approximately

$$\text{Log}L_{24} \approx \text{Log}L_{Ks} + 30.1 \quad (1)$$

(TBM09). (Here and in the following L_{24} and other MIPS luminosities are in erg s^{-1} and L_{Ks} are in solar units $L_{Ks,\odot}$.) A circumstellar origin for L_{24} in the old stellar populations in elliptical galaxies is based on the $r^{1/4}$ surface brightness profiles observed in both $24\mu\text{m}$ and Ks -band emission (Temi, Brighenti & Mathews 2008, hereafter TBM08). Whenever possible, the optical colors of early type galaxies in Figure 1 are designated with red or blue colors if $U - V$ exceeds 1.1 or not. Blue E and S0 galaxies are found only for $\text{Log}L_{Ks} \lesssim 11$, consistent with the much larger sample of Kannappan et al. (2009).

Relatively weak emission at 70 and $160\mu\text{m}$ from elliptical galaxies can be interpreted as emission from cold interstellar dust heated by diffuse starlight and thermal electrons in the hot interstellar gas (TMB07). Somewhat stronger emission at 70 and $160\mu\text{m}$ (as well as $24\mu\text{m}$) indicates either emission from dust that is buoyantly transported out from galactic cores by AGN feedback or, for the most infrared-luminous ellipticals, emission from large masses of dusty, star-forming gas apparently acquired in mergers with gas-rich galaxies. While a few S0 galaxies (open circles) occupy the same regions as the elliptical galaxies in Figure 1, the infrared luminosities of many S0 galaxies exceed those of E galaxies in all three Spitzer passbands.

While most representations of the Spitzer data result in broad scatter plots such as Figure 1, much tighter correlations emerge when the infrared luminosities are normalized by L_{Ks} as in Figure 2. Figure 2 significantly extends Figure 5 in TBM09² which does not continue above $\text{Log}L_{24}/L_{Ks} \approx 31$. In Figure 2 and subsequent figures we plot only

Spitzer detections, not upper limits.

The banana-shaped correlation in Figure 2 is driven by variations in the luminosity L_{Ks} of old stars and varying amounts of star-forming dusty gas. Most of the E galaxies and a few S0 galaxies with $\text{Log}L_{70}/L_{Ks}$ and $\text{Log}L_{160}/L_{Ks}$ less than ~ 31 have 24-Ks colors $\text{Log}L_{24}/L_{Ks} \approx 30.1$ characteristic of the spectral energy distribution (SED) of an old stellar population including circumstellar emission at $24\mu\text{m}$ (TBM09). We expect $\text{Log}L_{24}/L_{Ks}$ to asymptotically approach ~ 30.1 as $\text{Log}L_{FIR}/L_{Ks}$ decreases in Figure 2. It is unclear why the approach toward this final SED value is more complete in the horizontal distribution of red galaxies in the upper panel of Figure 2 than in the lower panel which may have a small residual positive slope when $\text{Log}L_{160}/L_{Ks} \lesssim 31$. Provided the infrared colors L_{24}/L_{70} and L_{160}/L_{24} are reasonably constant, galaxies with smaller L_{Ks} lie toward the upper right in both panels of Figure 2. Figure 3 is a second version of the data in Figure 2 that shows in detail how L_{Ks} varies along the correlations. While L_{Ks} decreases systematically toward the upper right in both panels of Figure 3, this trend is far from monotonic.

In Figure 2 we label the morphological type of early galaxies as either E or S0 while in practice morphological designations along the Hubble sequence are not rigorously discrete. In the Introduction we mentioned the uncertain morphological transition between E and S0 galaxies and the intermediate E-S0 type. As can be seen in Column 3 of Table 1, the transition from S0 to later type Sa galaxies is also gradual with S0-a (S0a or S0/a) galaxies bridging the transition. To explore the importance of these intermediate galaxy types, we examined plots similar to Figure 2 with early type galaxies binned by their specific HyperLeda morphology: E, E-S0, S0 and S0-a. For the relatively small numbers of galaxies in each subtype, we were unable to detect any difference between the distributions of S0 and S0-a galaxies in Figure 2, both types appear to be spread evenly along the entire color-color plot. The small number (~ 10) of E-S0 galaxies in Table 1 appear to be distributed as expected, sharing properties of both red and blue (E and S0) points in Figure 2. Consequently, in

²Apart from a constant, $\Delta\text{Log}(\lambda L_\lambda)_{24}$ in Figure 5 of TBM09 is essentially identical to $\text{Log}L_{24}/L_{Ks}$ used in this paper.

our plots we simply use the de Vaucouleurs $T = -3.0$ to separate E from S0 and regard all HyperLeda S0-a galaxies in Table 1 as S0 galaxies. Such distinctions are likely to be difficult or impossible for early type galaxies at high redshift.

To investigate further the origin of the tight correlations in Figures 2 and 3, we show in Figures 4a and 4b the independent variations of L_{Ks} and L_{24} with $\text{Log}L_{FIR}/L_{Ks}$, plotted along the horizontal axis exactly as in Figures 2 and 3. Figure 4a clearly reveals that the correlations in Figure 2 are largely a consequence of a pronounced decline in L_{Ks} . L_{Ks} can be considered a proxy for the mass of the old stellar population. But Figure 4b shows that the correlation in Figure 2 is also influenced by an increase in L_{24} . It is most interesting that the considerable scatter in Figures 4a and 4b is greatly reduced in Figure 2. Evidently values of both L_{24} and L_{Ks} for each galaxy conspire to ensure the much smaller scatter in Figure 2.

When $\text{Log}L_{24}/L_{Ks}$ sufficiently exceeds the old stellar population SED value 30.1 in Figure 2, $\text{Log}L_{24}/L_{Ks}$ becomes a measure of the specific star formation rate per unit L_{Ks} . In TBM09 we modified the expression for the star formation rate (SFR) based on $24\mu\text{m}$ emission from Calzetti et al. (2007) so that it is forced to become zero for old elliptical galaxies where circumstellar dust produces the $24\mu\text{m}$ emission, not star formation:

$$\begin{aligned} \text{SFR}(M_{\odot}, \text{yr}^{-1}) \\ = 1.24 \times 10^{-38} [\max(0.0, L_{24} - 10^{30.1} L_{Ks})]^{0.885}. \end{aligned} \quad (2)$$

This equation only applies when $\text{Log}L_{24}/L_{Ks}$ exceeds the range of values observed in old E galaxies, i.e. $\text{Log}L_{24}/L_{Ks} \gtrsim 30.5$ or

$$\text{SFR}(M_{\odot}, \text{yr}^{-1}) \gtrsim 0.044 (L_{24}/10^{11} L_{Ks,\odot})^{0.885}.$$

For those (mostly S0) galaxies in Figure 2 with $\text{Log}L_{24}/L_{Ks} \gtrsim 30.5$, the specific SFR per unit L_{Ks} increases with increasing $\text{Log}L_{24}/L_{Ks}$. This is consistent with the bluer colors of S0 galaxies in the upper part of the correlation in Figure 2 and with the “downsizing” notion that most current star formation is occurring in low- L_{Ks} galaxies (Cowie et al. 1996). Using equation (2), the star formation rates for the S0 galaxies having the largest L_{24} (top panel of Figure 1) is remarkably large: $1.4 \lesssim \text{SFR} \lesssim 11 M_{\odot} \text{yr}^{-1}$ for $43 \lesssim \text{Log}L_{24} \lesssim 44 \text{ erg s}^{-1}$.

5. Comparing Spitzer Observations of Early Type Galaxies with a More Morphologically Diverse Sample of Normal Galaxies

We now compare the results of our archival Spitzer sample of E and S0 galaxies with similar Spitzer observations of nearby normal galaxies spanning all morphological types. For this we use the SIRTIF Nearby Galaxy Survey or SINGS sample (Kennicutt et al. 2003) which has been extensively observed with Spitzer and other telescopes. Using data from Kennicutt et al. (2003) and the SINGS website, we plot in Figure 5 the SINGS Spitzer data in the same format as shown in the upper panels of Figures 2 and 4. In Figure 5 the SINGS galaxies are binned by morphological type designated by the HyperLeda designation of the de Vaucouleurs T parameter (upper panel) and by L_{Ks} (lower panel)³.

Figure 5 reveals that the morphological type of SINGS galaxies becomes progressively later (larger T) and the stellar luminosity L_{Ks} becomes smaller with increasing $\text{Log}L_{24}/L_{Ks}$, a measure of the star formation rate per L_{Ks} . Some of the morphological bins scatter along the correlation more than others and, as expected from Figure 2, this scatter is particularly large for SINGS S0 galaxies. Nevertheless, at least for some morphological types, it is remarkable that an approximate value of the type T can be inferred from L_{Ks} plus a single infrared observation of either 24, 70 or $160\mu\text{m}$. This single-color morphological identification is particularly effective for E ($-5 < T < -3$) and Sb-Sd ($3 < T < 7$) galaxies where the variation of L_{24}/L_{Ks} is more concentrated in Figure 5.

Dale et al. (2007) describe the detailed spectral energy distributions of the SINGS galaxies from UV to sub-millimeter wavelengths. We note that our Figure 5 is a somewhat simplified version of their Figure 10 where they plot a photometric measure of the specific star formation rate – a combination of UV emission from young stars with reprocessed infrared emission normalized by L_{Ks} – against the ratio of IR to UV light, also identify-

³The following ten galaxies are common to both the SINGS sample and ours (Table 1): NGC 584, 855, 1266, 1316, 1377, 1404, 3265, 4125, 4552 and 5866. In Figure 5 and subsequent figures that include galaxies from both samples, we plot these nine galaxies as members only of our sample.

ing each galaxy by its morphological type. Their figure lacks the banana simplicity of our Figure 5 in part because old population stars in early type galaxies can emit UV (and $24\mu\text{m}$) emission that is unrelated to the specific star formation rate.

In Figure 6 we combine the color-color plot of our sample of early type galaxies (as in Figure 2) with the SINGS galaxies now represented simply with black \times symbols. It is seen that galaxies of all morphological types and stellar masses lie along the same well defined banana-shaped correlation. In particular the S0 galaxies in our sample obey exactly the same correlation in the infrared color-color plot as the entire morphological sequence of normal galaxies, from ellipticals to irregulars. The coincidence of S0 infrared colors in Figure 6 with those of late-type SINGS galaxies, from spirals to irregulars, seems particularly surprising since cold gas in S0 galaxies is typically confined to small kpc-sized disks (e.g. Young, Bendo & Lucero 2009). Furthermore, S0 galaxies of varying L_{K_s} have star formation rates similar to spiral or irregular galaxies that are nearby in the infrared color-color plot (Fig. 6). However, the specific SFR that we refer to is based on observations of $\text{Log}L_{24}/L_{K_s}$ (eqn. 2), not Balmer emission line luminosities (Kennicutt et al. 2003) which, as least for the SAURON galaxies (TBM09), may not be as reliable in estimating the SFRs in S0 galaxies as in normal late type galaxies (Kennicutt et al. 2003).

In the upper panel of Figure 7 we compare galaxies from our early-type and the SINGS samples in a different way by over-plotting both samples as in the upper panel of Figure 1 but with L_{24} normalized with L_{K_s} . Using the symbol notation of Figure 1, the sample of early-type galaxies is shown as filled (E and E-S0) or open (S0 and later types) circles which are red or blue depending on the $U - V$ color. Early-type galaxies with unknown $U - V$ are shown with green symbols. The infrared color-magnitude diagram in the upper panel shows that galaxies are separated in an infrared red sequence (the horizontal strip at the bottom, locus of most ellipticals) and an infrared blue cloud, where almost all the SINGS galaxies and many S0s reside. The two sequences merge at the high luminosity end of our sample. About 24% of our early-type galaxies inhabit the infrared blue cloud. This result is consistent with the fraction of

not passive early-type galaxies in the COMA cluster estimated by Clemens et al. (2009) through the analysis of the $(K_s - [16\mu\text{m}])$ color-magnitude diagram.

The SINGS galaxies (black \times symbols in Fig. 7), occupy most of the same region as the early-type sample but extend to lower values of L_{K_s} , possibly reflecting a relative absence of low mass S0 galaxies. While this plot undoubtedly suffers from incompleteness and the multifarious nature of archived data, we see a gap or absence of galaxies with $30.5 \lesssim \text{Log}L_{24}/L_{K_s} \lesssim 31.25$ in the range $8.5 \lesssim \text{Log}L_{K_s} \lesssim 10$. However, the star formation rate would be very small for any galaxy that might exist in this gap. For example, at the upper boundary of this region devoid of galaxies $L_{24} \approx 10^{31.25} L_{K_s}$ and by equation (2) this corresponds to $SFR < 0.005(L_{K_s}/10^9 L_{K_s,\odot})^{0.885} M_{\odot} \text{yr}^{-1}$ which is very small indeed.

Figure 8 shows an optical color-magnitude diagram for our sample (and the SINGS sample) based on photometry from the website maintained by the Sloan Digital Sky Survey (SDSS). E, S0 and S0-a galaxies are shown respectively with red, green and blue symbols (no sample E/S0 galaxies have SDSS colors). The zero-redshift “red sequence” region is shown in Figure 8 as a solid line bracketed by an approximate $\pm 3\sigma$ dashed lines as found by Schawinski et al. (2009). Notice that S0 and S0-a galaxies appear to occupy approximately the same region in Figure 8 extending from the red sequence to the blue cloud region below, schematically shown as a shaded area (see Baldry et al., 2004, 2006). About 15% of early-type galaxies in our sample are in the blue cloud (see also Schawinski et al. 2009, Kannappan, Guie & Baker 2009). The lower panel of Figure 7 shows the corresponding infrared color-magnitude plot for galaxies in our sample and the SINGS sample (\times symbols) having SDSS colors plotted in Figure 8. The red (blue) symbols in the lower panel of Figure 7 represent galaxies that lie above (below) the lower dashed line in Figure 8. Symbols for E galaxies in this panel are filled and those for S0 or S0-a are open. What is striking about this panel is the relatively high specific star formation rates (larger $\text{Log}L_{24}/L_K$) for many galaxies that occupy the red-sequence region of Figure 8. Conversely, several galaxies that lie below the red sequence region in Figure 8 are seen to have red and dead infrared

colors in the lower panel of Figure 7, i.e. with $\text{Log}L_{24}/L_K$ typical of an old stellar population.

In Figure 9 we plot both samples in the $L_{24}/L_{70} - L_{70}/L_{160}$ color-color plot. Most SINGS galaxies in this plot have $L_{24}/L_{70} \approx -0.63 \pm 0.20$, resembling the L_{24}/L_{70} of early-type galaxies having low L_{24}/L_{70} . This plot suggests that the relative lack of scatter along the SINGS-sample correlation in Figure 5 is due in part to the general similarity of the L_{24}/L_{70} and L_{24}/L_{160} colors in dust emission temperatures among all galaxies.

6. Discussion

How closely do the galactic SFR and FIR luminosities depend on the mass of cold HI or H₂ gas? To answer this question we begin by plotting in Figure 10 the observed mass of HI and H₂ per unit L_{K_s} as a function of $\text{Log}L_{70}/L_{K_s}$, duplicating (the upper panel of) Figure 2 and Figure 5 but replacing L_{24} with M_{HI} and M_{H_2} . While correlations are clearly visible in Figure 10 – approximately with $M_{H_2}/L_K \propto L_{70}/L_K \propto M_{HI}/L_K$ – the scatter with M_{HI}/L_K (Fig. 10 upper panel) is significantly larger than those in Figures 2 and 5. The much lower scatter in the bottom panel of Figure 5 supports the widely accepted notion that stars form from molecular not atomic gas. Nevertheless, galaxies with similar L_{24} can have masses of molecular gas that vary over an order of magnitude. At fixed values of L_{70}/L_K the vertical scatter in Figure 2 is slightly less than that in the lower panel of Figure 10, suggesting that L_{24}/L_{K_s} is a better indicator of the specific SFR than M_{H_2}/L_{K_s} . Notice also that the SINGS galaxies occupy most of the same region in Figure 10 as the E and S0 galaxies in our sample, except near the upper and lower limits of the correlation.

In Figure 11 we explore this further by plotting L_{24} against the total mass of known cold gas $M_{gas} = M_{HI} + M_{H_2}$. It is seen that L_{24} can remain unchanged when M_{gas} varies by more than an order of magnitude and conversely, L_{24} can vary by 10-100 among galaxies with the same M_{gas} . The relationship between cold gas content and the SFR has a large scatter. Star-formation, as indicated by the 24 μ m emission, may be more sensitive to the local column density of molecular gas rather than its mean column density or total mass.

In principle the mass of cold gas and the star formation rate $\text{SFR}(t)$ can be used to estimate the time required to entirely consume the cold gas. An estimate of the gas consumption time is best done if we consider a subsample of S0 galaxies having similar morphologies and stellar mass. Consider, for example, an S0 galaxy with $L_{K_s} \approx 3 \times 10^{10} L_{K_s,\odot}$ and initial $L_{i,24}$ with $\text{Log}L_{i,24}/L_{K_s} \approx 43$ near the top of Figure 1 and suppose this galaxy initially contains cold gas of mass $M_i = M_{gas}$. Assume also that the galaxy forms stars at a rate $\text{SFR}(L_{24})$ given by equation (2) based on Calzetti et al. (2007). Setting aside the complication of mass return back to the interstellar medium from both young and old stars, the time required for all the gas to be consumed into stars is

$$t = \int_{L_{i,24}}^{L_{f,24}} \left(\frac{dM_{gas}}{dL_{24}} \right) \frac{dL_{24}}{\text{SFR}(L_{24})} \text{ yr} \quad (3)$$

where $\text{Log}(L_{f,24}/L_{K_s}) \approx 41$ is the maximum circumstellar emission expected from a gas-free S0 galaxy with $L_{K_s} \approx 3 \times 10^{10} L_{K_s,\odot}$ (Fig. 1). To estimate (dM_{gas}/dL_{24}) in equation (3) we plot in Figure 12 the observed $M_{gas}(L_{24})$ relation for galaxies having $10^{10} < L_{K_s} < 10^{11} L_{K_s,\odot}$. Unfortunately, it is clear from Figure 12 that the variation of dM_{gas}/dL_{24} with L_{24} is too uncertain to estimate the time required for the S0 galaxy to become “red and dead”. Evidently either (i) uncertainties in M_{gas} observations create too much scatter in Figure 12, (ii) rotationally supported cold gas in S0 galaxies having similar M_{gas} can be radially distributed in many different (post-merger?) ways, causing strong variations in local column density, the SFR and therefore L_{24} , or (iii) star formation may occur in a very intermittent fashion, causing L_{24} to have large variations for a given M_{gas} . Moreover, for some well-studied S0 galaxies with low SFRs the rate of stellar mass loss could in principle replenish cold gas at approximately the same rate that it is consumed by star formation (TBM09).

Nevertheless, since the uncertain slopes dM_{gas}/dL_{24} in Figures 10 and 11 appear to be quite large, it is possible that the star-formation rates in the cold gas are generally low and the gas-depletion times in S0 galaxies are long. The dusty star-forming regions in S0 galaxies are typically located in rotationally supported kpc-sized disks (e.g. Combes, Young & Bureau 2007; Young, Bureau & Cappel-

lari 2008 and Young, Bendo & Lucero 2009).

There is general agreement that at least some cold gas disks with masses $\sim 10^8 - 10^9 M_\odot$ in S0 galaxies arise as a result of mergers, as confirmed in a few cases by counter-rotation (e.g. Bertola et al. 1992; Kannappan & Fabricant 2001; Kannappan, Guie & Baker 2009; Sil’chenko, Moiseev & Afanasiev 2009). The statistical frequency of counter-rotating gas in early-type galaxies suggests that about half of them have acquired cold gas in a merger or related event (Kannappan & Fabricant 2001). To our knowledge no stars are observed to be counter-rotating with the cold gaseous S0 disks, but such observations might be possible by measuring the velocity of the absorption responsible for the $H\beta$ index. Evidently either the mergers are very recent or (more likely?) the mergers are quite old but the star formation rates are quite low. Although our data are sparse, the range of optical colors among the S0 galaxies in our sample is substantial, $-0.1 \lesssim U - V \lesssim 1.4$. If blue S0s acquired their cold gas more than a few Gyrs ago, they would be expected to exhibit a wide range of colors at high redshift, extending from the “red sequence” well into the “blue cloud”.

7. Conclusions

Our main conclusions are:

- (1) S0 galaxies are sources of a broad range of mid and far infrared emission. At the gas-free extreme, their emission at $24\mu\text{m}$ is circumstellar and emission at 70 and $160\mu\text{m}$ is likely to result from interstellar dust heated by diffuse starlight and the hot virialized interstellar gas (TMB07). However, many S0 galaxies appear to contain substantial masses of cold gas and dust which is heated by star formation and radiates at all Spitzer MIPS wavelengths. Using estimates of the star formation rate from the $24\mu\text{m}$ luminosity (Calzetti et al. 2007 and Eqn. 2), the most infrared-luminous S0 galaxies are currently forming stars at $1-10 M_\odot \text{yr}^{-1}$. Many S0s have blue $U - V$ colors consistent with recent star formation.
- (2) For our large sample of early-type E and S0 galaxies we find that infrared color-color diagrams with $\text{Log}(L_{24}/L_{Ks})$ plotted against $\text{Log}(L_{70}/L_{Ks})$ or $\text{Log}(L_{160}/L_{Ks})$ result in unusually tight correlations. At low values of

$\text{Log}(L_{70}/L_{Ks})$ or $\text{Log}(L_{160}/L_{Ks})$ these plots saturate at $\text{Log}(L_{24}/L_{Ks}) \approx 30.1$, corresponding to the typical SED for gas-free galaxies where there is no evidence for star formation and all the $24\mu\text{m}$ emission is circumstellar dust emission from old population giants. As the mass of cold dusty gas increases in S0 galaxies relative to that in the stars, $\text{Log}(L_{70}/L_{Ks})$ and $\text{Log}(L_{160}/L_{Ks})$ increase and the color-color correlations are elongated in the direction of decreasing L_{Ks} .

(3) Color-color plots of $\text{Log}(L_{24}/L_{Ks})$ against $\text{Log}(L_{70}/L_{Ks})$ or $\text{Log}(L_{160}/L_{Ks})$ for E and S0 galaxies are coincident with the same plots for normal nearby (non-active) galaxies in the SINGS sample (Kennicutt et al. 2003). Furthermore, the SINGS galaxies are arranged along the infrared color-color correlations approximately following the Hubble morphological sequence, $E \rightarrow \text{Sa} \rightarrow \text{Sc} \rightarrow \text{Im}$. An important exception to this are the S0 galaxies which are spread along the entire color-color correlation. The specific star formation rates per unit L_K (or stellar mass) for some S0 galaxies is comparable to those of spiral or irregular galaxies that lie near them in the infrared color-color plot (Fig. 2). The significant gas content in many S0 galaxies is likely to be relevant toward understanding the nature and origin of these galaxies.

(4) Far-infrared luminosities correlate only weakly with the mass of neutral and molecular hydrogen for SINGS galaxies and S0 galaxies from our sample. This suggests that star formation may be intermittent or that disks with nearly equal masses of cold gas are distributed differently with galactic radius in similar S0 galaxies so that the variation of local cold gas (volume and column) densities alters the local and global star formation rates.

(5) Early type galaxies do not have infrared properties that strictly adhere to the red sequence and blue cloud regions of the SDSS color magnitude plot. For example, in an IR color-magnitude plot quite a few galaxies in the SDSS red sequence occupy an infrared blue cloud region with larger $\text{Log}L_{24}/L_K$ than passively evolving ellipticals, indicating relatively high specific star formation rates. Conversely, a few galaxies occupying the green valley or blue cloud region of the SDSS color magnitude plot have infrared star formation

rates that are indistinguishable from pure gas-free, passively-evolving old stellar populations that define the infrared red sequence.

This work is based on observations made with the Spitzer Space Telescope, which is operated by the Jet Propulsion Laboratory, California Institute of Technology, under NASA contract 1407. This publication makes use of data products from the Two Micron All Sky Survey - which is a joint project of the University of Massachusetts and the Infrared Processing and Analysis Center/California Institute of Technology - and data from the Sloan Digital Sky Survey (SDSS). We acknowledge the usage of the HyperLeda database (<http://leda.univ-lyon1.fr>) and the NASA/IPAC Extragalactic Database (NED). Support for this work was provided by NASA through Spitzer Guest Observer grant RSA 1276023. Studies of the evolution of hot gas in elliptical galaxies at UC Santa Cruz are supported by NSF and NASA grants for which we are very grateful.

REFERENCES

- Baldry, I.K., Glazebrook, K., Brinkmann, J. et al. 2004, *ApJ*, 600, 681
- Baldry, I.K., Balogh, M.L., Bower, R.G., et al. 2006, *MNRAS*, 373, 469
- Bertola, F., Buson, L. M. & Zeilinger, W. W. 1992, *ApJ*, 401, L79
- Calzetti, D. et al. 2007, *ApJ*, 666, 870
- Clemens, M.S., Bressan, A., Panuzzo, P., et al. 2009, *MNRAS*, 392, 982
- Combes, F., Young, L. M., & Bureau, M. 2007, *MNRAS*, 377, 1795
- Cowie, L. L., Songaila, A., Hu, E. M. & Cohen, J. G. 1996, *AJ*, 112, 839
- Dale, D. A. et al., 2007, *ApJ*, 655, 863
- di Serego Alighieri, S. et al. 2007, *A&A*, 474, 851
- Donzelli, C.J. & Davoust, E. 2003, *A&A*, 409, 91
- Dubois P., Cambr esy L., 2003, *A&A*, 412, 45
- Engelbracht, C. W. et al. 2007, *PASP*, 119, 994
- Gordon, K. D., et al. 2007, *PASP*, 119, 1019
- Huchtmeier W. K. 1994, *A&A*, 286, 389
- Huchtmeier W. K. et al. 1995, *A&A*, 300, 675
- Kannappan, S. J., Guie, J. M. & Baker, A. J. 2009, (arXiv:0903.3695)
- Kannappan, S. J. & Fabricant, D. G. 2001, *AJ*, 121, 140
- Kennicutt, R. C. et al. 2003, *PASP*, 115, 928
- Kennicutt, R. C. et al. 2009, *ApJ* in press (arXiv:0908.0203)
- Knapp, G. R. & Raimond, E. 1984, *A&A*, 138, 77
- Lake G., Schommer, R. A., & Gorkom, J. H. 1987, *ApJ*, 314, 57
- Makovoz, D., Trey, R., Khan, L. & Booth, H. 2006 *Proc. SPIE*, 6274, 10
- Morganti, R., et al. 2006, *MNRAS*, 371, 157
- Nilson, P. 1973, *Uppsala General Catalogue of Galaxies, Nova Acta Regiae Societatis Scientiarum Upsaliensis, Ser. VA. vol. 1*
- Paturel G., Petit C., Prugniel P., Theureau G., Rousseau J., Brouty M.,
- Rieke, G. et al. 2004 *ApJS*, 154, 25
- Roberts, M. S. et al. 1991, *ApJS*, 75, 751
- Sage, L. J. & Welch, G. A., 2006, *ApJ*, 644, 850
- Sage L. J. et al. 2007, *ApJ*, 657, 232
- Sandler, E. M. et al. 2000, *AJ*, 119, 1180
- Schawinski, K. et al. 2009, *MNRAS*, 396, 818
- Sil'chenko, O. K., Moiseev, A. V. & Afanasiev, V. L. 2009, *ApJ*, 694, 1550
- Skrutskie, M. F., Cutri, R. M., Stiening, R. 2006, *AJ*, 131, 1163
- Stansberry, J. A. et al. 2007, *PASP*, 119, 1038
- Temi, P., Brighenti, F. & Mathews, W. G. 2009, *ApJ*, 695, 1
- Temi, P., Brighenti, F. & Mathews, W. G. 2008, *ApJ*, 672, 244
- Temi, P., Brighenti, F. & Mathews, W. G. 2007, *ApJ*, 666, 222
- Tonry, J. L. et al. 2001, *ApJ*, 546, 681
- Welch, G. A. & Sage, L. J. 2003, *ApJ*, 584, 260
- Werner, M. W. et al. 2004, *ApJS*, 154, 1
- Wiklind, T., Combes, F., and Henkel, C. 1995, *A&A*, 297, 643
- Young, L. M., Bendo, G. J. & Lucero, D. M. 2009, *AJ*, 137 3053

Young, L. M., Bureau, M. & Cappellari, M. 2008,
ApJ, 676. 317

Young, L. M. et al. 2002, ApJ, 124, 788

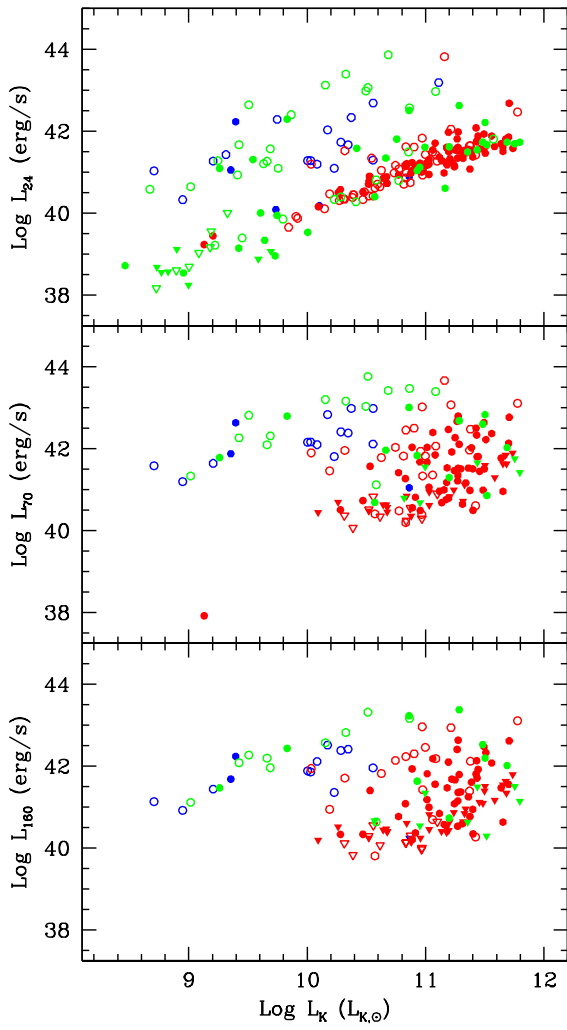


Fig. 1.— Spitzer data for elliptical and S0 galaxies. Circles represent observations, triangles upper limits. Filled symbols refer to elliptical galaxies with de Vaucouleurs classification parameter $T < -3$; open symbols refer to S0 galaxies with $T > -3$. Red (blue) symbols have optical colors $U - V < 1.1$ ($U - V > 1.1$); galaxies with unknown colors are plotted with green symbols.

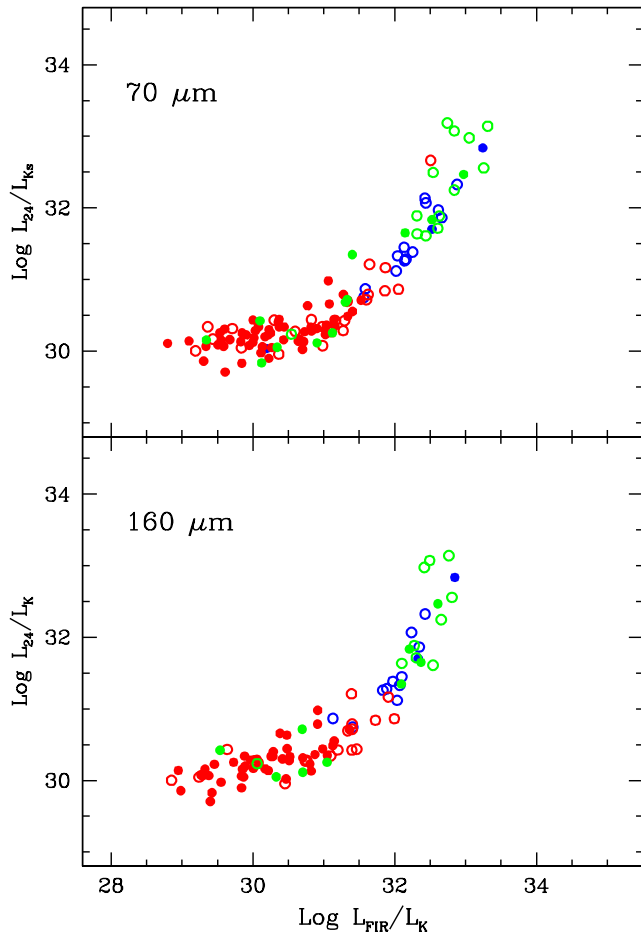


Fig. 2.— Infrared color-color plots of L_{24}/L_{Ks} against L_{70}/L_{Ks} (upper panel) and L_{160}/L_{Ks} (lower panel) for E (filled circles) and S0 (open circles) galaxies. Galaxies with red symbols have colors $U - V > 1.1$ indicating less star formation than those with blue symbols ($U - V < 1.1$). Green symbols identify galaxies for which optical colors are unavailable.

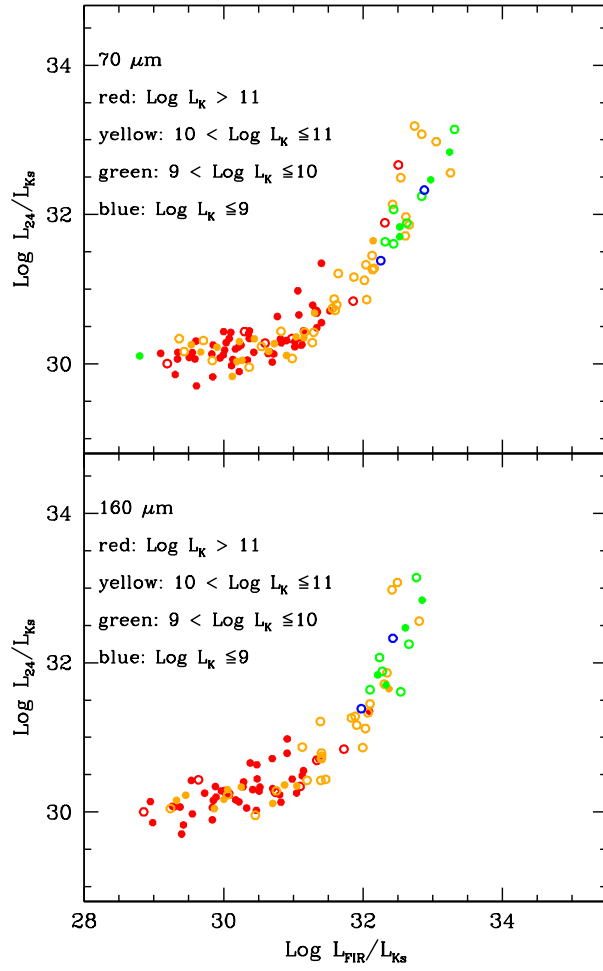


Fig. 3.— Infrared color-color plots of L_{24}/L_{Ks} against L_{70}/L_{Ks} and L_{160}/L_{Ks} for E (filled circles) and S0 (open circles) galaxies. Galaxies are color-binned with increasing L_{Ks} . The green galaxy to the far left in the upper panel is NGC 221 (M32).

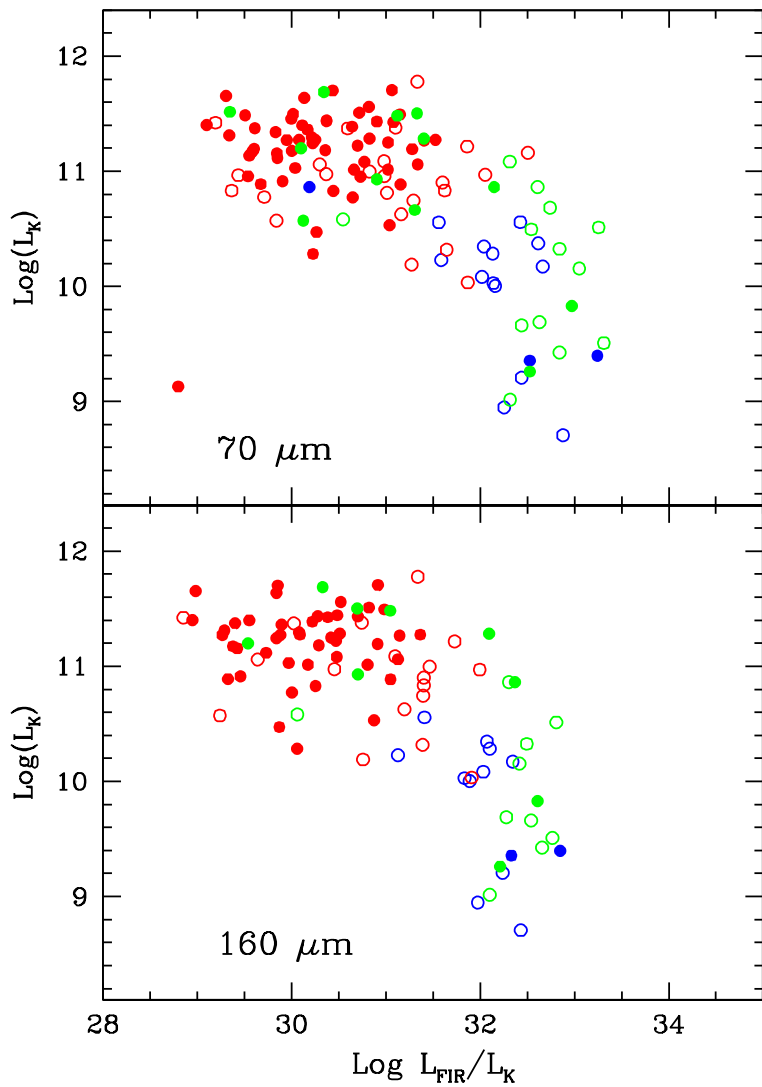


Fig. 4a.— Variation of L_{K_s} with $\text{Log}L_{FIR}/L_{K_s}$, the horizontal axis in Figure 2, where FIR represents 70 (upper panel) or $160\mu\text{m}$ (lower panel). Colors and symbols are identical to those in Figure 2. The red galaxy at the lower left in the upper panel is NGC 221 (M32).

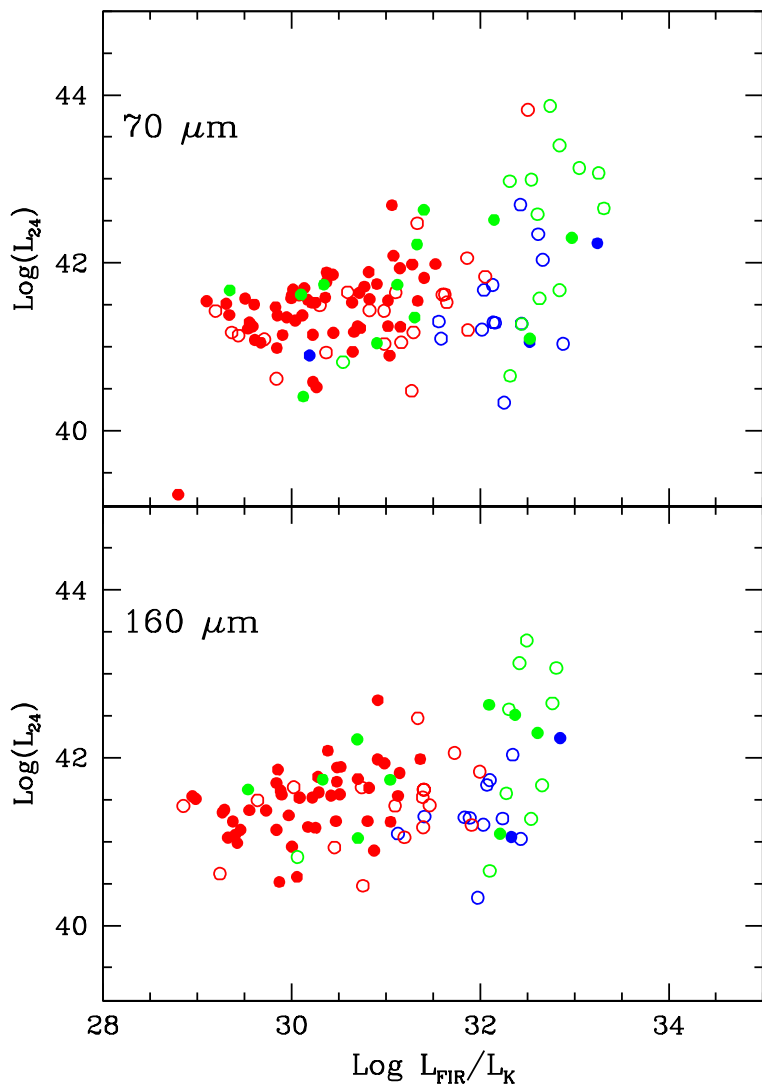


Fig. 4b.— Variation of L_{24} with $\text{Log}L_{FIR}/L_{Ks}$, the horizontal axis in Figure 2. Colors and symbols are identical to those in Figure 2. The red galaxy at the lower left in the upper panel is NGC 221 (M32).

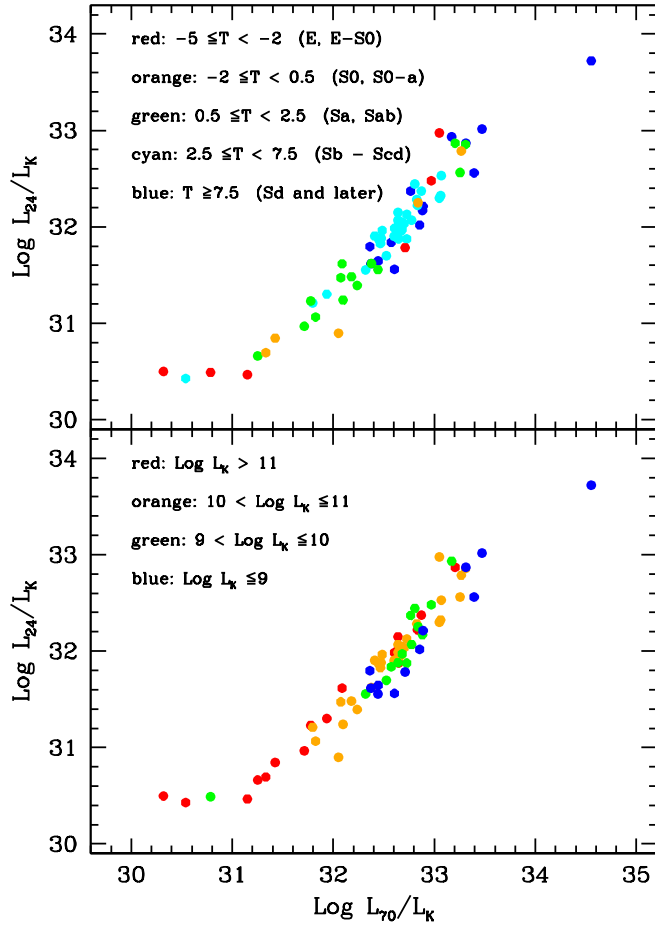


Fig. 5.— Spitzer data for SINGS galaxies. *Upper panel:* Color-binned by morphological T parameter. *Lower panel:* Color-binned in L_K .

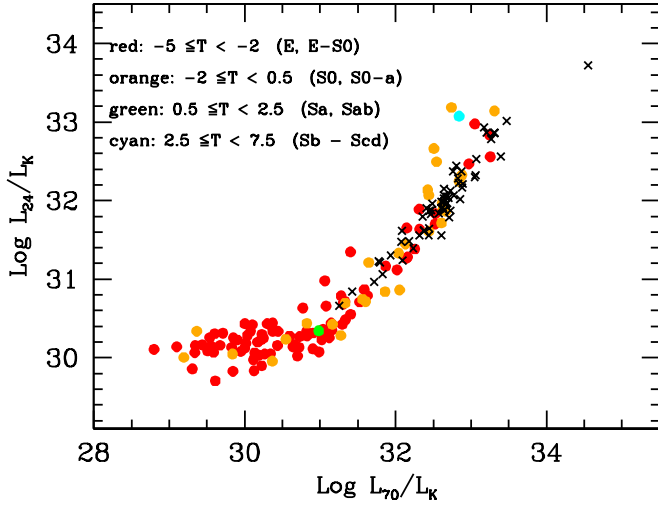


Fig. 6.— Infrared color-color plot for our sample of early-type galaxies combined with data for normal SINGS galaxies (not already in our sample) represented with black \times symbols.

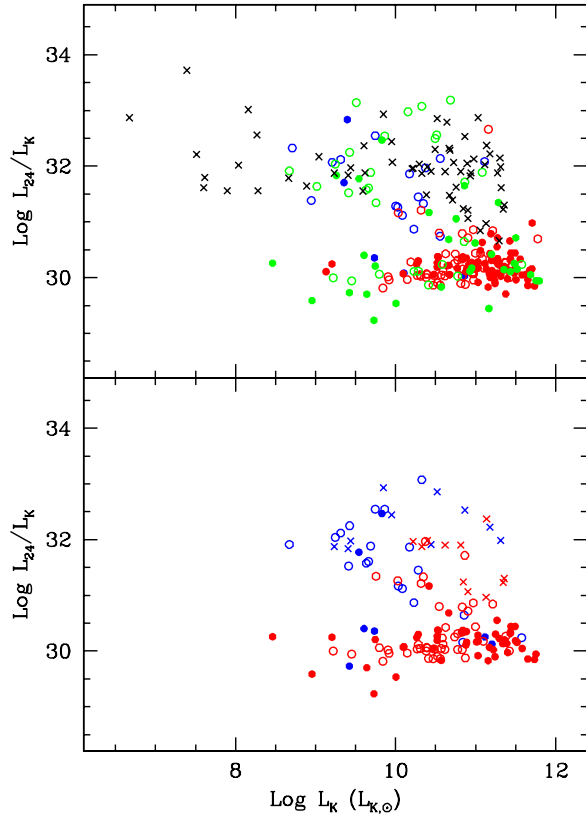


Fig. 7.— *Upper panel:* Combined plot of Spitzer data of early type galaxies from our sample and SINGS galaxies of all morphologies. Filled circles refer to elliptical galaxies with de Vaucouleurs classification parameter $T < -3$; open circles refer to S0 galaxies with $T > -3$. Red (blue) symbols have optical colors $U - V < 1.1$ ($U - V > 1.1$), and galaxies with unknown colors are not plotted. SINGS galaxies are represented with black \times symbols regardless of morphology. *lower panel:* A similar plot showing early-type galaxies from our sample together with the SINGS sample. Symbols are as in the upper panel except now red symbols indicate that the galaxies in our sample have $u - r$ colors that lie within 3σ of the zero-redshift SDSS red sequence while blue symbols correspond to galaxies with bluer $u - r$ colors.

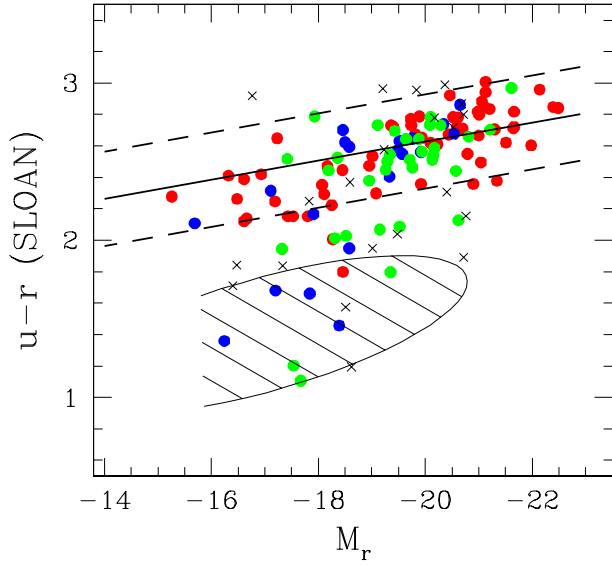


Fig. 8.— SDSS color-magnitude plot showing galaxies from our early-type sample and the SINGS sample. Only galaxies with SDSS colors are plotted. Red symbols are E galaxies (no sample E/S0 galaxies have SDSS colors), green are S0 galaxies and blue are S0-a galaxies. SINGS galaxies are represented with black \times symbols regardless of morphology. The solid line shows the zero-redshift red sequence defined as an approximate $\pm 3\sigma$ region bracketed with dashed lines. An approximate zero-redshift blue cloud region is shown below (shaded region).

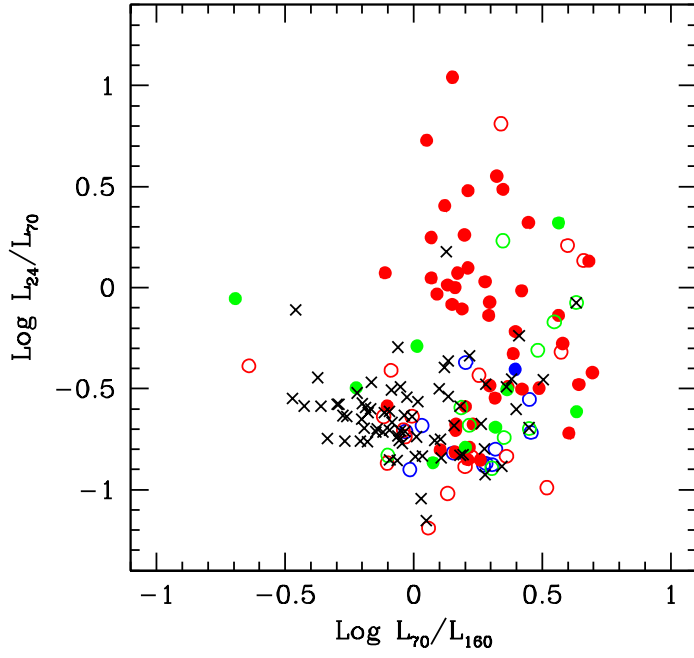


Fig. 9.— Combined color-color plot of early-type and SINGS galaxies (symbols as in Figure 7).

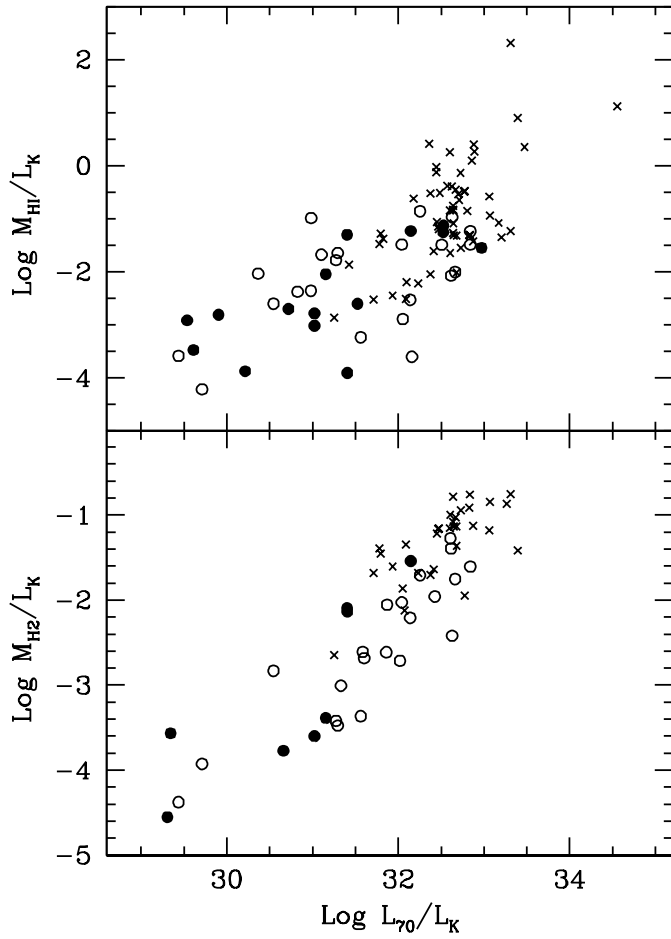


Fig. 10.— Plots of the mass of neutral and molecular cold gas per unit L_{K_s} against $\text{Log}L_{70}/L_{K_s}$, the horizontal axis in Figure 2 and Figure 5. Galaxies from our early type sample are designated with filled (E) or open (S0) circles; galaxies from the SINGS sample are shown with \times symbols.

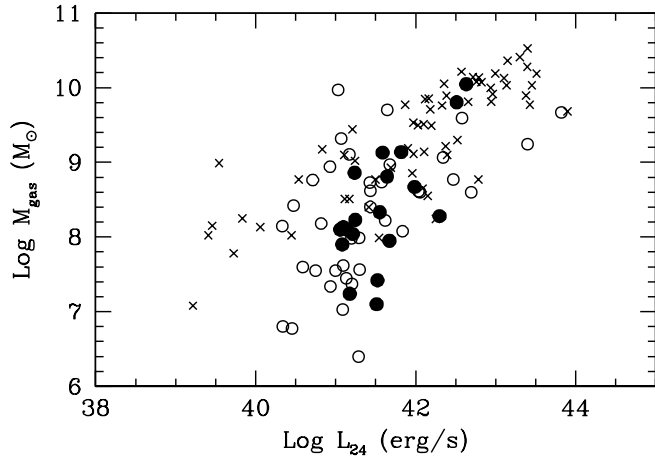


Fig. 11.— Plot of the total observed mass of cold gas $M_{gas} = M_{HI} + M_{H_2}$ against the $24\mu\text{m}$ luminosity. Galaxies from our early type sample are designated with filled (E) or open (S0) circles; galaxies from the SINGS sample are shown with \times symbols.

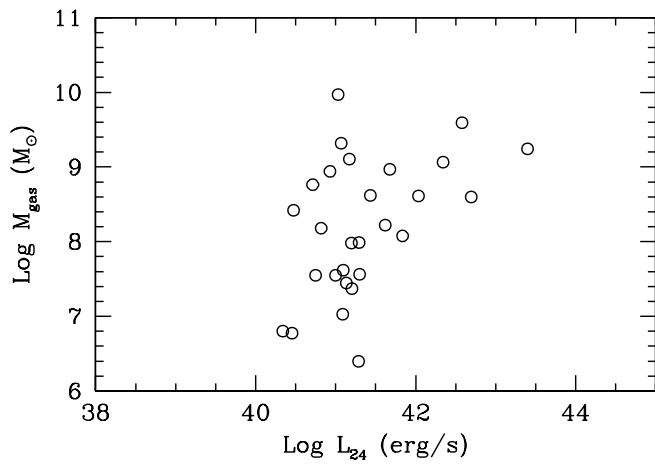


Fig. 12.— Similar to Figure 11, but restricted to S0 galaxies having $10 < \text{Log}L_{K_s} < 11$.

TABLE 1

| Name | PI/ID# | Type | T | D | Log L_{Ks} | U-V | Log M_{HI} | Log M_{H_2} | $F_{24\mu m}$ | $F_{70\mu m}$ | $F_{160\mu m}$ | Log $L_{24\mu m}$ | Log $L_{70\mu m}$ | Log $L_{160\mu m}$ |
|-------|-----------------|------|------|-------|---------------------|--------|-----------------|-----------------|---------------|---------------|----------------|-------------------|-------------------|--------------------|
| (1) | (2) | (3) | (4) | (Mpc) | ($L_{Ks, \odot}$) | (7) | (M_{\odot}) | (M_{\odot}) | (mJy) | (mJy) | (mJy) | ($erg\ s^{-1}$) | ($erg\ s^{-1}$) | ($erg\ s^{-1}$) |
| N0221 | Fazio/69 | E | -4.7 | 0.81 | 9.13 | 1.140 | ... | ... | 175±16 | 25±18 | ... | 39.24 | 37.93 | ... |
| N0315 | Fazio/69 | E | -4.0 | 58.88 | 13.44 | 1.487 | ... | ... | 94±6 | 331±17 | 536±48 | 42.69 | 42.77 | 42.62 |
| N0404 | Fazio/69 | E-SO | -2.8 | 3.27 | 8.95 | 1.095 | 8.09 | 7.24 | 135±8 | 2919±202 | 3499±366 | 40.33 | 41.20 | 40.92 |
| N0410 | Fazio/69 | E | -4.3 | 56.75 | 11.50 | 1.459 | ... | ... | 6.1±0.8 | ≤ 24 | ≤ 45 | 41.47 | ≤ 41.60 | ≤ 41.51 |
| N0474 | Zezas/20140 | SO | -2.0 | 33.46 | 10.98 | 1.157 | 8.94 | 7.63 | 5.1±2.2 | 38.2±7.5 | 107±22 | 40.93 | 41.34 | 41.43 |
| N0507 | Temi/20171 | E-SO | -3.3 | 67.19 | 11.68 | 1.364 | ... | ... | ... | ≤ 18.8 | ≤ 22.1 | ... | ≤ 41.64 | ≤ 41.35 |
| N0516 | Kannappan/30406 | SO-a | -1.5 | 35.01 | 10.22 | ... | ... | ... | 1.2±0.3 | ... | ... | 40.34 | ... | ... |
| N0526 | Werner/86 | SO | -2.0 | 78.70 | 3.14 | ... | ... | ... | 307±28 | 294±41 | ... | 43.45 | 42.97 | ... |
| N0533 | Temi/20171 | E | -4.8 | 68.23 | 11.64 | 1.495 | ... | ... | 7.2±3.1 | 24.8±4.9 | 28.7±5.6 | 41.70 | 41.77 | 41.48 |
| N0584 | Kennicutt/159 | E | -4.6 | 23.76 | 11.18 | 1.358 | ... | ... | 48.5±7.6 | 52.3±6.9 | ≤ 18.9 | 41.61 | 41.18 | 40.38 |
| N0596 | Surace/3403 | E | -4.3 | 23.87 | 10.91 | 1.239 | 8.1 | ... | 16.2±4.6 | 22.5±5.1 | 18.4±7.3 | 41.14 | 40.82 | 40.37 |
| N0636 | Surace/3403 | E | -4.8 | 22.28 | 10.67 | 1.372 | ... | 7.15 | 10.5±3.6 | ≤ 17.2 | ≤ 26.9 | 40.89 | 40.64 | 40.48 |
| N0720 | Temi/20171 | E | -4.8 | 22.29 | 11.14 | 1.410 | ... | 7.46 | 26.1±5.1 | 19.2±4.9 | ≤ 23.1 | 41.29 | 40.69 | 40.41 |
| N0777 | Fazio/69 | E | -4.8 | 55.21 | 11.49 | 1.524 | ... | ... | 8.2±2.7 | 6.3±2.8 | ≤ 18.4 | 41.57 | 40.99 | 41.10 |
| N0807 | Young/20780 | E | -4.8 | 69.18 | 11.28 | ... | 9.98 | 9.19 | 59.9±3.2 | 198±9 | 2233±235 | 42.63 | 42.69 | 43.38 |
| N0814 | Roussel/20577 | SO | -1.8 | 20.70 | 9.51 | ... | ... | ... | 697±42 | 3007±265 | 1952±182 | 42.65 | 42.82 | 42.27 |
| N0821 | Fabbiano/20371 | E | -4.8 | 24.09 | 10.95 | ... | ... | ... | 15.4±4.8 | ≤ 16.3 | ≤ 27.3 | 41.13 | 40.69 | 40.55 |
| N0855 | Kennicutt/159 | E | -4.6 | 9.33 | 9.35 | 0.613 | 8.10 | ... | 87.8±8.5 | 1700±136 | 2486±246 | 41.06 | 41.88 | 41.69 |
| N1016 | Fazio/30318 | E | -4.8 | 73.79 | 11.65 | 1.479 | ... | ... | 5.1±2.9 | ≤ 15.4 | ≤ 28.5 | 41.62 | 41.63 | 41.54 |
| N1023 | Fazio/69 | E-SO | -2.7 | 11.42 | 10.97 | 1.387 | 9.32 | 6.69 | 60.1±5.6 | ≤ 29.6 | ≤ 34.8 | 41.07 | 40.30 | 40.01 |
| N1199 | Johnson/3596 | E | -4.6 | 32.6 | 10.95 | 1.346 | ... | ... | 10.5±1.2 | 88±13 | ... | 41.22 | 41.68 | ... |
| N1266 | Kennicutt/40204 | SO | -2.1 | 30.06 | 10.51 | ... | ... | ... | 872±32 | 12690±535 | 10300±843 | 43.07 | 43.77 | 43.32 |
| N1316 | Kennicutt/159 | SO | -1.8 | 21.48 | 11.78 | 1.183 | ... | 8.77 | 430±21 | 5440±312 | 12610±886 | 42.47 | 43.11 | 43.11 |
| N1374 | Fazio/30318 | E | -4.3 | 19.77 | 10.68 | 1.347 | ... | ... | 9.2±1.4 | ≤ 18.5 | ≤ 28 | 40.73 | 40.57 | 40.39 |
| N1377 | Kennicutt/159 | SO | -2.1 | 22.20 | 10.15 | ... | ... | ... | 1835±84 | 6350±371 | 3380±248 | 43.13 | 43.20 | 42.57 |
| N1386 | Werner/86 | SO-a | -0.8 | 16.52 | 10.56 | 1.038 | ... | 8.60 | 1211±66 | 6900±412 | ... | 42.69 | 42.98 | ... |
| N1395 | Kaneda/3619 | E | -4.8 | 21.98 | 11.27 | 1.486 | ... | ... | 46.4±6.5 | 135±11 | 213±14 | 41.52 | 41.52 | 41.36 |
| N1399 | Temi/20171 | E | -4.5 | 19.40 | 11.40 | 1.429 | ... | ... | 61.9±7.3 | 16.4±7.6 | 26.5±8.6 | 41.54 | 40.50 | 40.35 |
| N1404 | Kennicutt/159 | E | -4.7 | 19.40 | 11.20 | 1.499 | ... | ... | 56.6±6.3 | 32.6±6.3 | ≤ 32.2 | 41.50 | 40.80 | 40.43 |
| N1407 | Kaneda/3619 | E | -4.5 | 22.08 | 11.36 | ... | ... | 7.55 | 43.4±6.4 | ≤ 21.1 | ≤ 38.9 | 41.50 | 40.74 | 40.63 |
| N1426 | Fazio/30318 | E | -4.6 | 24.10 | 10.64 | 1.292 | ... | ... | 8.3±2.1 | ≤ 14.4 | ≤ 21.4 | 40.86 | 40.63 | 40.44 |
| N1427 | Fazio/30318 | E | -4.0 | 23.55 | 2.09 | 1.300 | ... | ... | 9.5±1.4 | 27.3±1.1 | ≤ 13.3 | 40.90 | 40.89 | 40.22 |
| N1439 | Fazio/30318 | E | -4.7 | 26.67 | 10.77 | 1.207 | ... | ... | 8.2±0.8 | 72±6.2 | 37.5±8.0 | 40.94 | 41.42 | 40.78 |
| N1510 | Kennicutt/40204 | SO-a | -2.0 | 10.01 | 9.21 | 0.223 | ... | ... | 126±13 | 862±35 | 1237±103 | 41.28 | 41.65 | 41.44 |
| N1522 | Kennicutt/40204 | SO | -1.8 | 9.04 | 8.71 | -0.024 | ... | ... | 88±4 | 924±63 | 749±66 | 41.03 | 41.59 | 41.14 |
| N1533 | Putman/20695 | SO | -2.4 | 21.38 | 10.96 | 1.403 | 9.97 | ... | 15.8±2.3 | 374±18 | ... | 41.03 | 41.94 | ... |
| N1543 | Fisher/30496 | SO | -1.9 | 20.04 | 10.97 | 1.320 | ... | ... | 18.2±2.9 | ... | ... | 41.04 | ... | ... |
| N1553 | Fabbiano/20371 | SO | -2.3 | 18.54 | 11.37 | 1.301 | ... | ... | 86.7±8.9 | 527±24 | 322±21 | 41.65 | 41.97 | 41.39 |
| N1700 | Surace/3403 | E | -4.7 | 38.04 | 11.27 | 1.368 | ... | ... | 19.0±4.9 | 30.4±5.3 | 44.1±7.2 | 41.61 | 41.35 | 41.16 |
| N2110 | Werner/86 | E-SO | -3.0 | 31.33 | 11.08 | ... | ... | ... | 641±32 | 4966±422 | ... | 42.97 | 43.40 | ... |
| N2300 | Zezas/20140 | E-SO | -3.4 | 27.67 | 11.18 | 1.571 | ... | ... | 13.3±2.1 | ... | ... | 41.18 | ... | ... |
| N2325 | Temi/20171 | E | -4.7 | 31.92 | 11.20 | ... | ... | ... | 27.5±4.4 | 38.3±6.8 | 23.9±6.4 | 41.62 | 41.30 | 40.74 |
| N2434 | Fazio/30318 | E | -4.8 | 21.58 | 10.86 | 1.090 | ... | ... | 11.3±0.4 | 47.3±6.9 | ≤ 16.8 | 40.90 | 41.05 | 40.24 |
| N2685 | Rieke/40936 | SO-a | -1.1 | 15.63 | 10.39 | 1.029 | 9.26 | 7.50 | ... | ... | ... | ... | ... | ... |
| N2768 | Temi/20171 | E | -4.3 | 22.38 | 11.25 | 1.333 | 8.23 | 7.65 | 47.5±5.2 | 728±26 | 414±29 | 41.55 | 42.27 | 41.67 |
| N2778 | Fazio/30318 | E | -4.7 | 22.91 | 10.26 | 1.378 | ... | ... | 4.1±1.3 | ≤ 18.4 | ≤ 28.2 | 40.51 | 40.69 | 40.52 |
| N2787 | Fisher/30496 | SO-a | -1.1 | 7.48 | 10.19 | 1.396 | 8.41 | 6.77 | 36±5 | 1017±46 | 705±48 | 40.47 | 41.46 | 40.95 |
| N2832 | Fazio/69 | E | -4.3 | 85.90 | 11.74 | 1.447 | ... | ... | 3.5±0.5 | ≤ 21 | ≤ 38 | 41.59 | 41.90 | 41.80 |
| N2970 | Zezas/20140 | E | -4.6 | 25.23 | 9.74 | 0.868 | ... | ... | 1.3±0.2 | ... | ... | 40.09 | ... | ... |
| N2974 | Kaneda/3619 | E | -4.7 | 21.48 | 11.51 | 1.453 | 8.81 | 7.59 | 63.7±4.4 | 716±48 | 2076±154 | 41.64 | 42.23 | 42.33 |
| N2986 | Temi/20171 | E | -4.7 | 32.51 | 11.32 | 1.415 | ... | ... | 13.9±3.8 | ≤ 9.8 | ≤ 18.5 | 41.34 | 40.72 | 40.64 |
| N3011 | Kannappan/30406 | SO | -1.6 | 23.77 | 9.63 | ... | ... | ... | 19.2±3.2 | ... | ... | 41.21 | ... | ... |
| N3032 | Young/20780 | SO | -1.8 | 21.98 | 10.17 | 0.728 | 8.17 | 8.42 | 151±8 | 2772±184 | 3044±273 | 42.04 | 42.84 | 42.52 |
| N3073 | Fazio/69 | E-SO | -2.8 | 33.73 | 10.08 | 0.691 | ... | 7.37 | 9.4±1.5 | 218±8 | 515±42 | 41.20 | 42.10 | 42.12 |
| N3115 | Fazio/69 | E-SO | -2.9 | 9.68 | 10.97 | 1.375 | 7.38 | 6.48 | 97±4 | 52±4 | ≤ 45 | 41.13 | 40.40 | 39.98 |
| N3125 | Rieke/40936 | E | -4.8 | 13.43 | 9.40 | -0.118 | ... | ... | 636±32 | 4714±273 | 4337±327 | 42.23 | 42.64 | 42.24 |
| N3156 | Surace/3403 | SO | -2.4 | 22.39 | 10.23 | 0.924 | ... | 7.62 | 16.7±4.2 | 254±18 | 203±21 | 41.10 | 41.81 | 41.36 |
| N3226 | Appleton/1054 | E | -4.8 | 23.55 | 10.66 | ... | ... | ... | 26.9±3.2 | 327±14 | ... | 41.35 | 41.97 | ... |
| N3265 | Kennicutt/159 | E | -4.8 | 21.33 | 9.83 | ... | 8.28 | ... | 292±17 | 2719±144 | 2692±159 | 42.30 | 42.80 | 42.44 |
| N3377 | Fazio/69 | E | -4.8 | 11.22 | 10.47 | 1.102 | ... | 6.88 | 17.6±5.4 | 84.6±5.7 | 77.7±9.2 | 40.52 | 40.74 | 40.34 |
| N3379 | Fazio/69 | E | -4.8 | 10.57 | 10.89 | 1.436 | ... | 6.69 | 66.8±8.8 | 63.5±8.0 | 65.2±8.2 | 41.05 | 40.56 | 40.21 |
| N3384 | Surace/3403 | E-SO | -2.7 | 11.59 | 10.78 | 1.272 | 6.56 | 7.07 | 61.3±7.8 | 44.6±17.2 | ... | 41.09 | 40.49 | ... |

TABLE 1—Continued

| Name | PI/ID# | Type | T | D | Log L_{K_s} | U-V | Log M_{HI} | Log M_{H_2} | $F_{24\mu m}$ | $F_{70\mu m}$ | $F_{160\mu m}$ | Log $L_{24\mu m}$ | Log $L_{70\mu m}$ | Log $L_{160\mu m}$ |
|-------|-----------------|---------------------|------|-------|----------------------|-------|-----------------|-----------------|---------------|---------------|----------------|-------------------|-------------------|--------------------|
| (1) | (2) | (3) | (4) | (Mpc) | ($L_{K_s, \odot}$) | (7) | (M_{\odot}) | (M_{\odot}) | (mJy) | (mJy) | (mJy) | ($erg\ s^{-1}$) | ($erg\ s^{-1}$) | ($erg\ s^{-1}$) |
| N3412 | Fazio/69 | S0 | -2.0 | 11.32 | 10.39 | 1.193 | 6.20 | 6.64 | 14.9±1.9 | < 18 | < 24 | 40.45 | < 40.07 | < 39.84 |
| N3489 | Fazio/69 | S0-a | -1.3 | 12.08 | 10.56 | 1.082 | 7.32 | 7.19 | 91.6±6.7 | 1756±78 | 2814±128 | 41.30 | 42.12 | 41.96 |
| N3516 | Rieke/40936 | S0 | -2.0 | 38.37 | 11.11 | 0.649 | ... | ... | 712±32 | ... | ... | 43.19 | ... | ... |
| N3522 | Kannappan/30406 | E | -4.8 | 18.79 | 9.75 | ... | ... | ... | 1.7±0.3 | ... | ... | 39.95 | ... | ... |
| N3557 | Temi/20171 | E | -4.8 | 45.71 | 11.19 | 1.427 | ... | ... | 30.6±4.5 | 276±19 | 271±28 | 41.98 | 42.47 | 42.10 |
| N3585 | Fazio/69 | E | -4.7 | 20.04 | 11.27 | 1.357 | ... | ... | 37.2±3.8 | 80.2±5.2 | 38.2±8.2 | 41.35 | 41.22 | 40.54 |
| N3593 | Fazio/69 | S0-a | -0.4 | 9.91 | 10.37 | 1.082 | 8.30 | 8.98 | 1497±110 | 1.94e4±880 | ... | 42.34 | 42.99 | ... |
| N3607 | Fazio/69 | E-S0 | -3.1 | 22.80 | 11.27 | 1.360 | 7.36 | 9.13 | 84.9±6.7 | 1761±98 | 2215±186 | 41.82 | 42.67 | 42.41 |
| N3608 | Fazio/30318 | E | -4.8 | 22.91 | 10.83 | 1.284 | ... | 7.51 | 18.7±4.2 | 69.5±8.2 | 103±21 | 41.17 | 41.27 | 41.08 |
| N3610 | Surace/3403 | E | -4.2 | 29.24 | 11.12 | 1.293 | ... | ... | 18.4±4.5 | 21.1±7.3 | 36.5±16.5 | 41.37 | 40.97 | 40.84 |
| N3640 | Fazio/69 | E | -4.8 | 27.04 | 11.20 | 1.361 | ... | ... | 19.6±1.6 | < 18.3 | < 26.8 | 41.33 | < 40.84 | < 40.64 |
| N3656 | Young/20780 | Sa | -0.5 | 41.0 | 10.86 | ... | ... | 9.59 | 151±0.2 | 3447±179 | 3911±295 | 42.58 | 43.47 | 43.17 |
| N3706 | Fazio/30318 | E-S0 | -3.3 | 37.21 | 11.33 | 1.398 | ... | ... | 16.5±4.4 | < 18.6 | < 22.3 | 41.53 | < 41.12 | < 40.84 |
| N3773 | Kennicutt/40204 | S0 | -2.0 | 15.07 | 9.43 | ... | 7.94 | ... | 139±9 | 1591±183 | 2379±232 | 41.67 | 42.27 | 42.08 |
| N3870 | Kannappan/30406 | S0 | -2.0 | 14.03 | 9.31 | 0.177 | 8.22 | 7.94 | 92.1±5.1 | ... | ... | 41.43 | ... | ... |
| N3923 | Temi/20171 | E | -4.6 | 19.14 | 11.31 | 1.442 | ... | ... | 43.7±6.7 | 23.8±5.4 | 48.4±7.8 | 41.38 | 40.65 | 40.60 |
| N3941 | Rieke/40936 | S0 | -2.0 | 12.19 | 10.59 | 1.272 | 8.74 | 7.44 | 23.3±3.1 | ... | ... | 40.71 | ... | ... |
| N3945 | Fazio/30318 | S0-a | -1.2 | 21.37 | 11.00 | 1.380 | 8.62 | ... | 39.9±4.1 | 284±19 | 2836±216 | 41.43 | 41.82 | 42.46 |
| N3962 | Kaneda/3619 | E | -4.7 | 23.23 | 11.01 | 1.354 | 8.23 | ... | 21.8±5.6 | 392±18 | 544±24 | 41.24 | 42.03 | 41.82 |
| N4026 | Fazio/30318 | S0 | -1.8 | 13.61 | 10.58 | ... | 7.98 | 7.75 | 23.7±3.0 | 141±13 | 106±23 | 40.82 | 41.13 | 40.64 |
| N4073 | Fazio/30318 | E | -4.1 | 79.43 | 11.75 | ... | ... | ... | 5.3±3.0 | < 17.7 | < 22.6 | 41.70 | < 41.76 | < 41.50 |
| N4117 | Kannappan/30406 | S0 | -2.0 | 16.35 | 9.76 | ... | ... | ... | 31.4±3.4 | ... | ... | 41.10 | ... | ... |
| N4125 | Kennicutt/159 | E | -4.8 | 27.79 | 11.49 | 1.377 | ... | ... | 74.7±6.9 | 1105±98 | 1735±187 | 41.94 | 42.64 | 42.48 |
| N4138 | Fazio/69 | S0-a | -0.8 | 13.8 | 10.35 | 1.038 | 8.86 | 8.32 | 167±16 | 2505±162 | 6144±642 | 41.68 | 42.39 | 42.42 |
| N4150 | Fazio/69 | S0 ⁰ (r) | -2.1 | 13.74 | 10.00 | 1.016 | 7.50 | 7.82 | 69.3±8 | 1522±121 | 1720±168 | 41.29 | 42.17 | 41.86 |
| N4168 | Fazio/69 | E | -4.8 | 33.73 | 11.03 | 1.318 | ... | ... | 5.2±1.3 | < 15 | < 26 | 40.95 | < 40.94 | < 40.82 |
| N4203 | Fazio/69 | E-S0 | -2.7 | 15.14 | 10.75 | 1.387 | 9.10 | 7.27 | 43.3±3.5 | 933±111 | 2701±259 | 41.17 | 42.04 | 42.14 |
| N4251 | Fazio/69 | S0 | -1.9 | 19.59 | 10.84 | 1.200 | 7.55 | 7.41 | 17.3±2.4 | ... | ... | 41.00 | ... | ... |
| N4261 | Rieke/40936 | E | -4.8 | 31.62 | 11.44 | 1.464 | ... | ... | 51.5±3.2 | 127±11 | 375±18 | 41.89 | 41.81 | 41.92 |
| N4267 | Cote/3649 | E-S0 | -2.7 | 15.92 | 10.62 | 1.382 | ... | ... | 11.7±0.3 | < 16.9 | < 20.9 | 40.65 | < 40.34 | < 40.07 |
| N4278 | Fazio/69 | E | -4.8 | 16.07 | 10.88 | 1.319 | 8.84 | 7.50 | 44.7±12.7 | 829±68 | 1491±128 | 41.24 | 42.04 | 41.94 |
| N4291 | Tripp/30603 | E | -4.8 | 26.18 | 10.82 | ... | ... | ... | < 18 | ... | ... | ... | < 40.08 | ... |
| N4308 | Kannappan/30406 | E | -4.7 | 11.29 | 9.21 | 1.107 | ... | ... | 1.49±0.3 | ... | ... | 39.45 | ... | ... |
| N4344 | Popescu/3475 | S0 | -1.7 | 17.85 | 9.66 | ... | ... | ... | 39.2±4.5 | 773±62 | 2228±226 | 41.27 | 42.10 | 42.20 |
| N4350 | Cote/3649 | S0 | -1.8 | 15.92 | 10.63 | 1.292 | ... | ... | 29.8±3.3 | 474±32 | 1168±112 | 41.05 | 41.79 | 41.82 |
| N4352 | Treu/30958 | S0 | -2.0 | 30.96 | 10.38 | 1.349 | ... | ... | 1.7±0.3 | ... | ... | 40.39 | ... | ... |
| N4365 | Cote/3649 | E | -4.8 | 17.06 | 11.16 | 1.411 | ... | ... | 22.2±4.7 | 67.0±8.0 | 58.2±7.3 | 40.98 | 41.00 | 40.58 |
| N4371 | Cote/3649 | S0-a | -1.3 | 14.32 | 10.57 | 1.549 | ... | ... | 13.6±0.7 | 24.5±2.7 | 14.1±7.0 | 40.62 | 40.41 | 39.81 |
| N4374 | Rieke/82 | E | -4.2 | 18.37 | 11.38 | 1.594 | ... | 7.15 | 66.6±8.6 | 617±41 | 535±61 | 41.53 | 42.03 | 41.61 |
| N4377 | Treu/30958 | E-S0 | -2.6 | 21.26 | 10.47 | 1.292 | ... | ... | 3.2±0.3 | ... | ... | 40.33 | ... | ... |
| N4379 | Treu/30958 | E-S0 | -2.8 | 14.19 | 10.15 | 1.269 | ... | ... | 4.3±0.3 | ... | ... | 40.11 | ... | ... |
| N4382 | Cote/3649 | S0-a | -1.3 | 18.45 | 11.42 | 1.220 | ... | 7.34 | 52.4±6.7 | 23.6±6.5 | 24.7±9 | 41.43 | 40.61 | 40.27 |
| N4386 | Tripp/30603 | S0 | -2.0 | 27.04 | 10.81 | 1.331 | ... | ... | ... | 178±14 | ... | ... | 41.82 | ... |
| N4406 | Fazio/69 | E | -4.7 | 17.14 | 11.37 | 1.527 | 7.90 | ... | 27.5±3.2 | 64±8 | 90±12 | 41.08 | 40.98 | 40.77 |
| N4417 | Treu/30958 | S0 | -1.9 | 15.92 | 10.48 | 1.183 | ... | ... | 8.8±1.2 | ... | ... | 40.52 | ... | ... |
| N4421 | Fazio/69 | S0-a | -0.2 | 23.12 | 10.56 | 1.116 | ... | ... | 3.3±0.4 | < 25 | < 30 | 40.42 | < 40.84 | < 40.56 |
| N4434 | Treu/30958 | E | -4.8 | 26.79 | 10.52 | 1.262 | ... | ... | 4.8±0.9 | ... | ... | 40.71 | ... | ... |
| N4435 | Cote/3649 | S0 | -2.1 | 15.92 | 10.83 | 1.508 | ... | ... | 111±10.2 | 2210±186 | 3022±327 | 41.62 | 42.46 | 42.23 |
| N4442 | Fazio/69 | S0 | -2.0 | 8.68 | 10.31 | 1.392 | ... | ... | 20.2±2.2 | ... | ... | 40.36 | ... | ... |
| N4458 | Fazio/30318 | E | -4.8 | 17.22 | 10.10 | 1.152 | ... | 7.28 | 3.3±1.1 | < 18.5 | < 23.8 | 40.16 | < 40.45 | < 40.20 |
| N4459 | Cote/3649 | S0-a | -1.4 | 16.14 | 10.90 | 1.481 | ... | 8.22 | 107±8 | 2400±175 | 3461±431 | 41.62 | 42.51 | 42.31 |
| N4460 | Fazio/69 | S0-a | -0.9 | 9.59 | 9.69 | ... | 8.72 | 7.27 | 27.4±31 | 4413±389 | 4488±461 | 41.58 | 42.32 | 41.97 |
| N4464 | Treu/30958 | S0-a | -0.7 | 15.92 | 9.92 | 1.341 | ... | ... | 2.0±0.3 | ... | ... | 39.88 | ... | ... |
| N4472 | Fazio/69 | E | -4.8 | 17.06 | 11.65 | 1.461 | ... | 7.10 | 74.7±8.6 | 61.1±7.6 | 66.4±7.8 | 41.51 | 40.96 | 40.64 |
| N4473 | Cote/3649 | E | -4.7 | 15.71 | 10.88 | 1.504 | ... | 7.01 | 26.3±6.7 | < 18.0 | < 25.5 | 40.99 | < 40.36 | < 40.15 |
| N4474 | Treu/30958 | S0 | -2.0 | 15.92 | 10.27 | 1.246 | ... | ... | 5.4±0.8 | ... | ... | 40.31 | ... | ... |
| N4476 | Young/20780 | E-S0 | -3.0 | 17.22 | 10.03 | 1.159 | ... | 7.98 | 35.7±4.1 | 528±89 | 1323±135 | 41.20 | 41.90 | 41.94 |
| N4477 | Rieke/40936 | S0 | -1.9 | 17.06 | 10.87 | 1.649 | ... | 7.55 | 12.9±3.2 | < 24 | < 31 | 40.75 | < 40.55 | < 40.31 |
| N4478 | Fazio/30318 | E | -4.8 | 18.11 | 10.52 | 1.477 | ... | ... | 12.6±3.9 | < 17.9 | < 23.7 | 40.79 | < 40.48 | < 40.24 |
| N4479 | Treu/30958 | S0 | -1.8 | 15.92 | 9.84 | 1.386 | ... | ... | 1.2±0.3 | ... | ... | 39.66 | ... | ... |
| N4482 | Treu/30958 | E | -4.8 | 27.83 | 10.00 | ... | ... | ... | 0.3±0.16 | ... | ... | 39.54 | ... | ... |
| N4483 | Treu/30958 | S0-a | -1.3 | 13.69 | 9.91 | 1.217 | ... | ... | 3.0±0.3 | ... | ... | 39.92 | ... | ... |

TABLE 1—Continued

| Name | PI/ID# | Type | T | D | Log L_{K_s} | U-V | Log M_{HI} | Log M_{H_2} | $F_{24\mu m}$ | $F_{70\mu m}$ | $F_{160\mu m}$ | Log $L_{24\mu m}$ | Log $L_{70\mu m}$ | Log $L_{160\mu m}$ |
|-------|-----------------|------|------|-------|----------------------|-------|-----------------|-----------------|---------------|---------------|----------------|-------------------|-------------------|--------------------|
| (1) | (2) | (3) | (4) | (Mpc) | ($L_{K_s, \odot}$) | (7) | (M_{\odot}) | (M_{\odot}) | (mJy) | (mJy) | (mJy) | ($erg\ s^{-1}$) | ($erg\ s^{-1}$) | ($erg\ s^{-1}$) |
| N4486 | Cote'/3649 | E | -4.3 | 16.07 | 11.44 | 1.648 | ... | 7.03 | 154±9 | 483±44 | 896±91 | 41.77 | 41.81 | 41.71 |
| N4489 | Treu/30958 | E | -4.8 | 17.86 | 10.10 | 1.053 | ... | ... | 3.2±0.3 | ... | ... | 40.18 | ... | ... |
| N4494 | Fazio/69 | E | -4.8 | 17.06 | 11.01 | 1.284 | ... | 7.24 | 34.5±4.5 | 316±12.5 | 235±19.6 | 41.18 | 41.67 | 41.19 |
| N4515 | Treu/30958 | E-SO | -3.0 | 15.92 | 9.80 | ... | ... | ... | 1.9±0.2 | ... | ... | 39.86 | ... | ... |
| N4526 | Fazio/69 | SO | -1.9 | 16.90 | 11.21 | 1.354 | ... | 8.60 | 267±12 | 8134±632 | 13706±1267 | 42.06 | 43.08 | 42.94 |
| N4528 | Treu/30958 | SO | -2.0 | 20.76 | 10.39 | 1.346 | ... | ... | 4.4±0.7 | ... | ... | 40.45 | ... | ... |
| N4552 | Kennicutt/159 | E | -4.6 | 15.34 | 11.03 | 1.625 | ... | 7.18 | 58.5±7.8 | 96.3±10.2 | 188±16 | 41.31 | 41.06 | 41.00 |
| N4564 | Fabbiano/20371 | E | -4.8 | 15.00 | 10.53 | 1.484 | ... | ... | 23.9±3.7 | ... | ... | 40.90 | ... | ... |
| N4570 | Cote'/3649 | SO | -2.0 | 25.90 | 11.10 | 1.253 | ... | 7.75 | 18.7±6.0 | < 23.3 | < 29.6 | 41.27 | < 40.90 | < 40.65 |
| N4578 | Fazio/69 | SO | -2.0 | 18.54 | 10.52 | 1.123 | ... | ... | 5.2±0.9 | < 19 | < 26 | 40.43 | < 40.52 | < 40.30 |
| N4589 | Kaneda/3619 | E | -4.8 | 21.98 | 10.93 | ... | ... | ... | 15.3±4.5 | 275±16 | 396±21 | 41.04 | 41.83 | 41.63 |
| N4612 | Fazio/69 | SO | -2.0 | 26.61 | 10.77 | ... | ... | ... | 6.0±0.8 | ... | ... | 40.80 | ... | ... |
| N4621 | Cote'/3649 | E | -4.8 | 18.28 | 11.17 | 1.354 | ... | ... | 34.9±6.3 | 33.7±5.7 | 47.4±6.6 | 41.24 | 40.76 | 40.55 |
| N4623 | Treu/30958 | SO-a | -1.5 | 26.62 | 10.41 | ... | ... | ... | 1.8±0.2 | ... | ... | 40.28 | ... | ... |
| N4636 | Fazio/69 | E | -4.8 | 17.06 | 11.24 | 1.319 | ... | 6.85 | 31.8±5.6 | 197±12 | 185±24 | 41.14 | 41.47 | 41.08 |
| N4638 | Fazio/69 | E-SO | -2.6 | 21.68 | 10.74 | 1.290 | ... | ... | 13.9±2.8 | ... | ... | 40.99 | ... | ... |
| N4649 | Fazio/69 | E | -4.6 | 17.06 | 11.52 | ... | ... | 7.78 | 108±10 | 48.6±6.8 | < 30.4 | 41.67 | 40.86 | < 40.30 |
| N4660 | Cote'/3649 | E | -4.7 | 12.82 | 10.28 | 1.268 | ... | ... | 15.5±4.3 | 38.3±6.2 | 59.1±8.2 | 40.58 | 40.51 | 40.43 |
| N4694 | Kenney/30945 | SO | -2.0 | 18.17 | 10.28 | 0.737 | ... | ... | 110±9 | 1545±112 | 3278±334 | 41.73 | 42.42 | 42.38 |
| N4696 | Sparks/3506 | E | -3.7 | 39.65 | 11.69 | ... | ... | ... | 23.4±4.7 | 133±13 | 295±21 | 41.74 | 42.03 | 42.02 |
| N4697 | Surace/3403 | E | -4.8 | 16.22 | 11.22 | 1.237 | ... | 7.16 | 44.7±6.7 | 618±55 | 830±68 | 41.24 | 41.92 | 41.69 |
| N4709 | Fazio/30318 | E | -4.4 | 35.32 | 11.24 | 1.397 | ... | ... | 8.2±0.2 | < 15.5 | < 27.0 | 41.18 | < 41.00 | < 40.88 |
| N4754 | Cote'/3649 | SO | -2.5 | 16.83 | 10.83 | 1.275 | ... | ... | 17.1±2.9 | < 12.2 | < 22.2 | 40.86 | < 40.25 | < 40.15 |
| N4762 | Cote'/3649 | SO | -1.8 | 15.92 | 10.83 | 1.141 | ... | ... | 39.1±6.5 | 12.1±2.6 | 24.2 | 41.17 | 40.20 | 40.14 |
| N4786 | Fazio/30318 | E | -4.2 | 66.16 | 11.50 | ... | ... | ... | 25.3±1.2 | 303±26.0 | 161±19 | 42.22 | 42.83 | 42.20 |
| N4915 | Surace/3403 | E | -4.5 | 46.98 | 11.18 | 1.251 | ... | ... | 11.7±5.5 | 30.6±4.8 | 59.7±8.9 | 41.59 | 41.54 | 41.47 |
| N4936 | Fazio/30318 | E | -4.6 | 41.07 | 11.48 | ... | ... | ... | 21.7±0.9 | 465±45.0 | 894±76.0 | 41.74 | 42.60 | 42.53 |
| N5018 | Surace/3403 | E | -4.6 | 32.36 | 11.27 | 1.207 | 8.67 | ... | 61.7±9.1 | 1174±134 | 1855±241 | 41.98 | 42.80 | 42.64 |
| N5044 | Temi/20171 | E | -4.7 | 32.36 | 11.28 | 1.389 | ... | ... | 23.5±5.3 | 241±23 | 266±28 | 41.57 | 42.11 | 41.80 |
| N5061 | Fazio/30318 | E | -4.3 | 18.28 | 10.96 | 1.209 | 8.04 | ... | 32.8±0.5 | 18.2±5.2 | < 23.5 | 41.21 | 40.49 | < 40.25 |
| N5077 | Fazio/69 | E | -4.8 | 32.36 | 11.08 | 1.488 | ... | ... | 33.2±5.7 | 133±11 | 155±18 | 41.72 | 41.85 | 41.56 |
| N5173 | Kannappan/30406 | E | -4.7 | 34.99 | 10.42 | ... | 9.13 | ... | 21.1±1.5 | ... | ... | 41.59 | ... | ... |
| N5273 | Fazio/69 | SO | -1.9 | 16.52 | 10.32 | 1.132 | ... | ... | 83.1±4.5 | 657±44 | 836±79 | 41.53 | 41.96 | 41.71 |
| N5322 | Fazio/69 | E | -4.8 | 29.79 | 11.43 | 1.345 | ... | ... | 42.2±6.4 | 477±23 | 687±77 | 41.75 | 42.34 | 42.14 |
| N5338 | Kannappan/30406 | SO | -2.0 | 12.82 | 9.41 | ... | 7.34 | ... | 35.2±5.0 | ... | ... | 40.94 | ... | ... |
| N5353 | Fazio/69 | SO | -2.1 | 34.67 | 11.38 | 1.480 | 9.70 | ... | 24.7±3.3 | 492±38 | 490±52 | 41.65 | 42.48 | 42.12 |
| N5419 | Fazio/30318 | E | -4.4 | 53.44 | 11.80 | ... | ... | ... | 12.9±0.14 | < 18.3 | < 21.7 | 41.74 | < 41.43 | < 41.14 |
| N5481 | Zezas/20140 | E | -4.0 | 30.75 | 10.57 | ... | ... | ... | 1.8±0.3 | 10.2±3.4 | < 22 | 40.41 | < 40.69 | < 40.67 |
| N5557 | Surace/3403 | E | -4.8 | 49.02 | 11.50 | 1.386 | ... | ... | 13.4±5.0 | 26.4±7.5 | 19.6 | 41.68 | 41.51 | 41.39 |
| N5576 | Surace/3403 | E | -4.8 | 25.47 | 11.03 | 1.224 | ... | ... | 16.5±4.2 | < 12.7 | < 19.8 | 41.20 | < 40.63 | < 40.46 |
| N5596 | Kannappan/30406 | SO | -1.8 | 47.80 | 10.54 | 1.219 | ... | ... | 6.5±0.5 | ... | ... | 41.35 | ... | ... |
| N5666 | Young/20780 | Sc | 6.4 | 33.45 | 10.33 | ... | 9.09 | 8.72 | 1503±0.5 | 2566±155 | 2637±244 | 43.40 | 43.17 | 42.82 |
| N5813 | Fazio/69 | E | -4.8 | 32.21 | 11.40 | 1.418 | ... | 7.64 | 15.3±4.9 | 61.3±7.6 | 38.3±5.9 | 41.37 | 41.51 | 40.95 |
| N5831 | Surace/3403 | E | -4.8 | 27.16 | 10.84 | 1.427 | ... | 7.79 | 14.8±4.6 | < 18.8 | < 24.6 | 41.21 | < 40.85 | < 40.61 |
| N5845 | Fabbiano/20371 | E | -4.8 | 25.94 | 10.53 | 1.674 | ... | 7.45 | 7.8±3.2 | 108±12 | 169±23 | 40.89 | 41.57 | 41.41 |
| N5846 | Fazio/69 | E | -4.7 | 24.89 | 11.36 | 1.370 | ... | 7.72 | 39.3±6.2 | 107±10 | 129±12 | 41.56 | 41.53 | 41.25 |
| N5866 | Kennicutt/159 | SO-a | -1.2 | 15.35 | 10.97 | 1.108 | 8.08 | 8.64 | 194±7.1 | 8753±605 | 17537±1297.0 | 41.83 | 43.02 | 42.97 |
| N5982 | Surace/3403 | E | -4.8 | 40.18 | 11.30 | 1.354 | 7.42 | 7.53 | 13.8±5.1 | 39.0±7.2 | 65.8±11.7 | 41.52 | 41.51 | 41.38 |
| N6482 | Fazio/69 | E | -4.8 | 54.69 | 2.82 | 1.054 | ... | ... | 9.5±0.8 | 33.6±12.1 | < 45.2 | 41.63 | 41.71 | < 41.48 |
| N6684 | Fisher/30496 | SO | -1.8 | 13.93 | 10.82 | 1.189 | ... | ... | 17.7±2.0 | ... | ... | 40.71 | ... | ... |
| N6703 | Fazio/69 | E-SO | -2.8 | 32.06 | 11.06 | 1.360 | ... | ... | 20.3±4.5 | 43.5±6.4 | 21.7±5.1 | 41.49 | 41.36 | 40.70 |
| N6776 | Fazio/30318 | E | -4.1 | 70.41 | 11.43 | 1.293 | ... | ... | 16.4±1.3 | 126±12 | 58.1±19.3 | 42.08 | 42.50 | 41.81 |
| N6849 | Fazio/30318 | E-SO | -3.3 | 84.41 | 11.44 | ... | ... | ... | 3.3±0.1 | < 12.6 | < 19.8 | 41.55 | < 41.66 | < 41.50 |
| N7077 | Kannappan/30406 | E | -4.1 | 17.06 | 9.26 | ... | 8.13 | ... | 28.7±3.1 | 411±37 | 452±42 | 41.10 | 41.79 | 41.47 |
| N7176 | Johnson/3596 | E | -4.6 | 32.39 | 11.16 | ... | ... | ... | 2.6±0.4 | ... | ... | 40.61 | ... | ... |
| N7360 | Kannappan/30406 | E | -5.0 | 67.30 | 10.76 | ... | ... | ... | 9.6±0.6 | ... | ... | 41.81 | ... | ... |
| N7457 | Fazio/30318 | E-SO | -2.6 | 13.24 | 10.32 | 1.113 | 6.25 | 6.66 | 8.4±2.5 | < 25.9 | < 33.5 | 40.34 | < 40.37 | < 40.12 |
| N7619 | Temi/20171 | E | -4.7 | 52.97 | 11.58 | 1.430 | ... | ... | 10.2±4.7 | < 13.7 | < 23.5 | 41.63 | < 41.29 | < 41.17 |
| N7626 | Fazio/30318 | E | -4.8 | 39.99 | 11.34 | 1.459 | ... | ... | 12.4±3.6 | 18±0.3 | 25.3 | 41.47 | 41.17 | 40.96 |
| N7785 | Fazio/30318 | E | -4.8 | 55.46 | 11.46 | 1.449 | ... | ... | 8.2±0.7 | 18±0.9 | 19.0 | 41.58 | 41.45 | < 41.12 |
| I0798 | Treu/30958 | E | -4.4 | 7.66 | 8.46 | ... | ... | ... | 0.6±0.2 | ... | ... | 38.72 | ... | ... |

TABLE 1—Continued

| Name | PI/ID# | Type | T | D | Log L_{Ks} | U-V | Log M_{HI} | Log M_{H_2} | $F_{24\mu m}$ | $F_{70\mu m}$ | $F_{160\mu m}$ | Log $L_{24\mu m}$ | Log $L_{70\mu m}$ | Log $L_{160\mu m}$ |
|---------|-----------------|------|------|--------|---------------------|-------|-----------------|-----------------|---------------|---------------|----------------|-------------------|-------------------|--------------------|
| (1) | (2) | (3) | (4) | (Mpc) | ($L_{Ks, \odot}$) | (7) | (M_{\odot}) | (M_{\odot}) | (mJy) | (mJy) | (mJy) | ($erg\ s^{-1}$) | ($erg\ s^{-1}$) | ($erg\ s^{-1}$) |
| I1144 | Kannappan/30406 | E-S0 | -3.0 | 176.20 | 11.57 | ... | ... | ... | 1.4±0.3 | ... | ... | 41.81 | ... | ... |
| I1459 | Latter/1712 | E | -4.7 | 29.24 | 11.56 | 1.449 | ... | ... | 60.9±4.3 | 542±32 | 627±72 | 41.89 | 42.38 | 42.08 |
| I1639 | Kannappan/30406 | E-S0 | -3.0 | 75.86 | 10.86 | ... | ... | ... | 3.7±0.4 | ... | ... | 41.50 | ... | ... |
| I3032 | Treu/30958 | E? | -2.4 | 18.26 | 9.00 | ... | ... | ... | ∞ | ∞ | ∞ | 38.70 | ... | ... |
| I3101 | Treu/30958 | E? | -2.5 | 31.67 | 9.18 | ... | ... | ... | ∞ | ∞ | ∞ | 39.18 | ... | ... |
| I3328 | Treu/30958 | E-S0 | -2.9 | 15.71 | 9.22 | ... | ... | ... | 0.45±0.08 | ... | ... | 39.22 | ... | ... |
| I3370 | Kaneda/3619 | E | -4.7 | 26.79 | 11.06 | 1.186 | ... | ... | 32.8±3.4 | 680±51 | 958±128 | 41.55 | 42.40 | 42.19 |
| I3381 | Treu/30958 | E | -4.1 | 10.85 | 9.00 | ... | ... | ... | ∞ | ∞ | ∞ | 38.24 | ... | ... |
| I3383 | Treu/30958 | E? | -2.7 | 27.05 | 9.08 | ... | ... | ... | ∞ | ∞ | ∞ | 39.04 | ... | ... |
| I3461 | Treu/30958 | E | -4.1 | 15.60 | 8.77 | 0.30 | ... | ... | ∞ | ∞ | ∞ | 38.56 | ... | ... |
| I3468 | Treu/30958 | E | -4.8 | 19.62 | 9.73 | ... | ... | ... | 0.16±0.08 | ... | ... | 38.96 | ... | ... |
| I3470 | Treu/30958 | E | -4.0 | 22.71 | 9.59 | ... | ... | ... | ∞ | ∞ | ∞ | 38.89 | ... | ... |
| I3487 | Treu/30958 | E-S0 | -2.9 | 16.60 | 8.90 | ... | ... | ... | ∞ | ∞ | ∞ | 38.61 | ... | ... |
| I3501 | Treu/30958 | E | -4.2 | 24.76 | 9.64 | ... | ... | ... | 0.24±0.08 | ... | ... | 39.34 | ... | ... |
| I3586 | Treu/30958 | S0-a | -0.8 | 26.06 | 9.33 | ... | ... | ... | ∞ | ∞ | ∞ | 40.01 | ... | ... |
| I3602 | Treu/30958 | E | -5.0 | 31.43 | 9.61 | ... | ... | ... | 0.69±0.11 | ... | ... | 40.01 | ... | ... |
| I3633 | Treu/30958 | E | -3.6 | 29.87 | 8.90 | ... | ... | ... | ∞ | ∞ | ∞ | 39.12 | ... | ... |
| I3652 | Treu/30958 | E | -4.8 | 10.32 | 8.96 | ... | ... | ... | 0.22±0.08 | ... | ... | 38.54 | ... | ... |
| I3653 | Treu/30958 | S0 | -2.2 | 14.72 | 9.45 | ... | ... | ... | 0.77±0.12 | ... | ... | 39.40 | ... | ... |
| I3735 | Treu/30958 | E | -3.5 | 28.08 | 9.69 | ... | ... | ... | ∞ | ∞ | ∞ | 39.07 | ... | ... |
| I3773 | Treu/30958 | E | -4.8 | 16.71 | 9.42 | ... | ... | ... | 0.34±0.08 | ... | ... | 39.15 | ... | ... |
| I3779 | Treu/30958 | E | -5.0 | 17.92 | 8.73 | ... | ... | ... | ∞ | ∞ | ∞ | 38.68 | ... | ... |
| I4296 | Fabbiano/20371 | E | -4.8 | 47.56 | 11.70 | 1.426 | ... | ... | 21.4±8 | 118±12 | 71±12 | 41.86 | 42.14 | 41.56 |
| I4329 | Fazio/30318 | E | -3.8 | 61.97 | 10.99 | ... | ... | ... | 7.2±1.5 | ∞ | ∞ | 41.62 | ∞ | 41.35 |
| I5063 | Werner/86 | S0-a | -0.9 | 45.29 | 11.16 | 1.268 | 9.67 | ... | 2170±78 | 4425±321 | ... | 43.82 | 43.67 | ... |
| E103-35 | Werner/86 | S0-a | -0.3 | 54.20 | 10.68 | ... | ... | ... | 1693±81 | 1774±112 | ... | 43.87 | 43.43 | ... |
| E428-14 | Werner/86 | S0 | -1.7 | 21.27 | 10.50 | ... | ... | ... | 1448±80 | 4714±389 | ... | 42.99 | 43.04 | ... |
| E462-15 | Fazio/30318 | E | -4.8 | 84.41 | 11.68 | 1.264 | ... | ... | 6.1±0.7 | ∞ | ∞ | 41.81 | 41.85 | 41.63 |
| E483-13 | Kennicutt/40204 | E-S0 | -2.8 | 10.05 | 9.02 | ... | ... | ... | 29.8±3.8 | 417±23 | 579±69 | 40.65 | 41.33 | 41.12 |
| U1503 | Young/20780 | E | -4.8 | 74.13 | 10.86 | ... | 9.63 | 9.32 | 39.6±1.8 | 362±66 | 1384±139 | 42.51 | 43.01 | 43.23 |
| U6570 | Kannappan/30406 | S0-a | -0.2 | 25.35 | 9.86 | ... | ... | ... | 266±33 | ... | ... | 42.41 | ... | ... |
| U6637 | Kannappan/30406 | E-S0 | -3.4 | 27.76 | 9.54 | ... | ... | ... | 18.±2.3 | ... | ... | 41.32 | ... | ... |
| U6655 | Kannappan/30406 | S0-a | -0.3 | 11.86 | 8.67 | ... | 7.60 | ... | 18.4±6 | ... | ... | 40.59 | ... | ... |
| U6805 | Kannappan/30406 | S0-a | -1.2 | 17.49 | 9.25 | ... | ... | ... | 42.±3.6 | ... | ... | 41.28 | ... | ... |
| U7020A | Kannappan/30406 | S0-a | -1.5 | 25.21 | 9.75 | 0.303 | ... | ... | 207±12 | ... | ... | 42.29 | ... | ... |
| U7399A | Treu/30958 | S0 | -2.5 | 22.64 | 2.06 | ... | ... | ... | ∞ | ∞ | ∞ | 38.88 | ... | ... |
| U7436 | Treu/30958 | S0-a | -1.0 | 15.49 | 9.19 | ... | ... | ... | ∞ | ∞ | ∞ | 39.55 | ... | ... |
| U7580 | Treu/30958 | S0-a | -1.5 | 9.95 | 8.73 | ... | ... | ... | ∞ | ∞ | ∞ | 38.17 | ... | ... |
| U7854 | Treu/30958 | E | -3.5 | 15.88 | 8.83 | ... | ... | ... | ∞ | ∞ | ∞ | 38.58 | ... | ... |
| U8876 | Kannappan/30406 | S0-a | -0.1 | 33.57 | 10.29 | ... | ... | ... | 1.5±0.3 | ... | ... | 40.40 | ... | ... |

NOTES: The columns are as follows: Column (1). – Galaxy name. N = NGC, I = IC, E = ESO, U = UGC. Column (2). – Principal Investigator (PI) and Program Identification number (ID#) of the Spitzer observing programs from which galaxies have been selected.

Column (3). – Galaxy morphological type (Hubble type) from the HyperLeda Database. Column (4). – De Vaucouleurs numerical type, T. Its correspondence with the Hubble type is defined in RC2. Data values are taken from the HyperLeda Database. Column (5). – Galaxy distance. When available, distances are taken from Tonry et al. (2001), otherwise they are from the NASA

Extragalactic Database (NED) and corrected for $H_0 = 70\text{ km s}^{-1}\text{ Mpc}^{-1}$. Column (6). – Luminosities in the Ks band, L_{Ks} , have been derived using the flux density F_{Ks} published by the 2MASS survey, Skrutskie et al. (2006). Column (7). – U-V colors have been derived from the U-B and B-V colors listed in the HyperLeda database. Column (8). – The neutral hydrogen masses, M_{HI} are taken from the following publications: Morganti et al. (2006); Sage & Welch (2006); Di Serego et al. (2007); Roberts et al. (1991);

Huchtmeier (1994); Huchtmeier et al. (1995); Sadler et al. (200); Knapp & Raimond (1984). Column (9). – Molecular gas masses, M_{H_2} are collected from the following publications: Combes et al. (2007); Young et al. (2009); Young et al. (2002); Sage et al. (2007); Welch & Sage (2003); Roberts et al. (1991). Column (10-12). – MIPS flux densities at 24, 70 and 160 μm . Column (13-15). – Specific luminosities L_{λ} at 24, 70 and 160 μm . In this paper L_{λ} represents λL_{λ} in erg s^{-1} . This differs from our previous notation in which

L_{λ} represented the Spitzer band width multiplied by the specific luminosity.